České vysoké učení technické v Praze

Fakulta jaderná a fyzikálně inženýrská

Katedra fyziky

Studium interakce těžkých kvarků s jadernou hmotou ve srážkách Cu+Cu při $\sqrt{s_{NN}} = 200$ GeV

Diplomová práce

Autor: Miroslav Krůs

Vedoucí práce: Mgr. Jaroslav Bielčík, Ph.D.

Akademický rok: **2007/2008**

Czech Technical University in Prague

Faculty of Nuclear Sciences and Physical Engineering

Department of Physics

Study of Interaction of Heavy Quarks with Nuclear Matter in Cu+Cu at $\sqrt{s_{NN}} = 200$ GeV

Diploma Thesis

Author: Miroslav Krůs

Supervisor: Mgr. Jaroslav Bielčík, Ph.D.

Academic year: **2007/2008**

Název práce:
Studium interakce těžkých kvarků s jadernou hmotou ve srážkách Cu+Cu při $\sqrt{s_{NN}} = 200$ GeV

Autor: Miroslav Krůs

Obor: Experimentální jaderná fyzika

Druh práce: Diplomová práce

Vedoucí práce: Mgr. Jaroslav Bielčík, Ph.D., Katedra fyziky, FJFI, ČVUT v Praze.

Abstrakt: Experimentální výsledky získané na urychlovači RHIC v BNL ukázaly, že potlačení produkce těžkých mezonů v centrálních srážkách Au+Au při $\sqrt{s_{NN}} = 200$ GeV je podobné potlačení produkce lehčích mezonů. Záměrem této práce je studium interakce těžkých kvarků s prostředím vytvořeným při srážkách Cu+Cu při energii $\sqrt{s_{NN}} = 200$ GeV. Těžké kvarky mohou být studovány prostřednictvím elektronů vznikajících při slabých rozpadech těchto kvarků. V této práci jsme se zaměřili na studium zmeny tvaru v azimutálních korelacích elektronů s hadrony při úhlu 180^o. Podobná struktrura byla pozorována v azimutálních korelačních funkcích lehkých hadronů ve srážkách Au+Au.

Klíčová slova: těžké kvarky , STAR, azimutální korelace, nefotonické elektrony, srážky těžkých iontů, kvark gluonové plazma, Machův kužel

Title:
Study of Interaction of Heavy Quarks with Nuclear Matter in Cu+Cu at $\sqrt{s_{NN}} = 200$ GeV

Abstract: The experimental results at RHIC in the BNL, shows that suppression of heavy mesons production in the central Au+Au collisions at $\sqrt{s_{NN}} = 200$ GeV is similar to the suppression of production of lighter mesons. The aim of this work is to study the interaction of heavy quarks with a medium produced in the Cu+Cu collisions at $\sqrt{s_{NN}} = 200$ GeV. Heavy quarks can be studied via electrons coming from their weak decays. In this work, we have focused on the study of the modification of the away-side peak in the electron-hadron azimuthal correlations. Such modification was observed in light di-hadron correlations in Au+Au collisions.

Key words: heavy quarks, heavy flavor, STAR, azimuthal correlations, non-photonic electron, heavy ion collisions, quark gluon plasma, Mach cone

Acknowledgments

First of all, I am very grateful to my supervisor Jaro Bielčík for his invaluable help, movation, encouragement, patience, and guidance through the preparation of this work. I would like to thank Jana Bielčíková for introduction into azimuthal correlation method. I am also very thankful to Anders Knospe and Christine Nattrass for their help with data analysis software. Special thanks are due to Pavel Janík and Radek Šmakal for language corrections.

Contents

List of Figures

Introduction

Experimental investigations of dense and hot nuclear matter produced in laboratory in ultrarelativistic nucleus-nucleus collisions is common interest to nuclear physics, particle physics, astrophysics and cosmology.

During last fifteen years there have been several dedicated experiments build at SPS in CERN in Switzerland and RHIC in BNL in USA for systematic investigation of signals related to this new state of matter - quark gluon plasma - to understand its properties.

In this work we investigate the Cu+Cu collisions at $\sqrt{s_{NN}} = 200$ GeV measured in STAR at RHIC. We focuse on azimuthal correlations of non-photonic electrons with hadrons in order to learn about medium response to passage of heavy quarks.

After the introduction to quark gluon plasma in Chapter 1 and introduction to measure the heavy quarks in Chapter 2, we describe the RHIC facility and STAR detector in Chapter 3. In Chapter 4, we present the details of the analysis and in Chapter 5, we present the results and conclusion.

Chapter 1

Quark Gluon Plasma

The fundamental theory describing interactions among quarks and gluons is called Quantum Chromodynamics (QCD)[1]. Free quarks have never been observed, this is a consequence of fact that the interaction between quarks and gluons is increasing with their separation. This phenomenon is known as the confinement of quarks and gluons inside hadrons. At very short distances (much shorter than size of hadrons) the QCD coupling constant between the quarks decreases, this phenomenon is known as asymptotic freedom [2, 3].

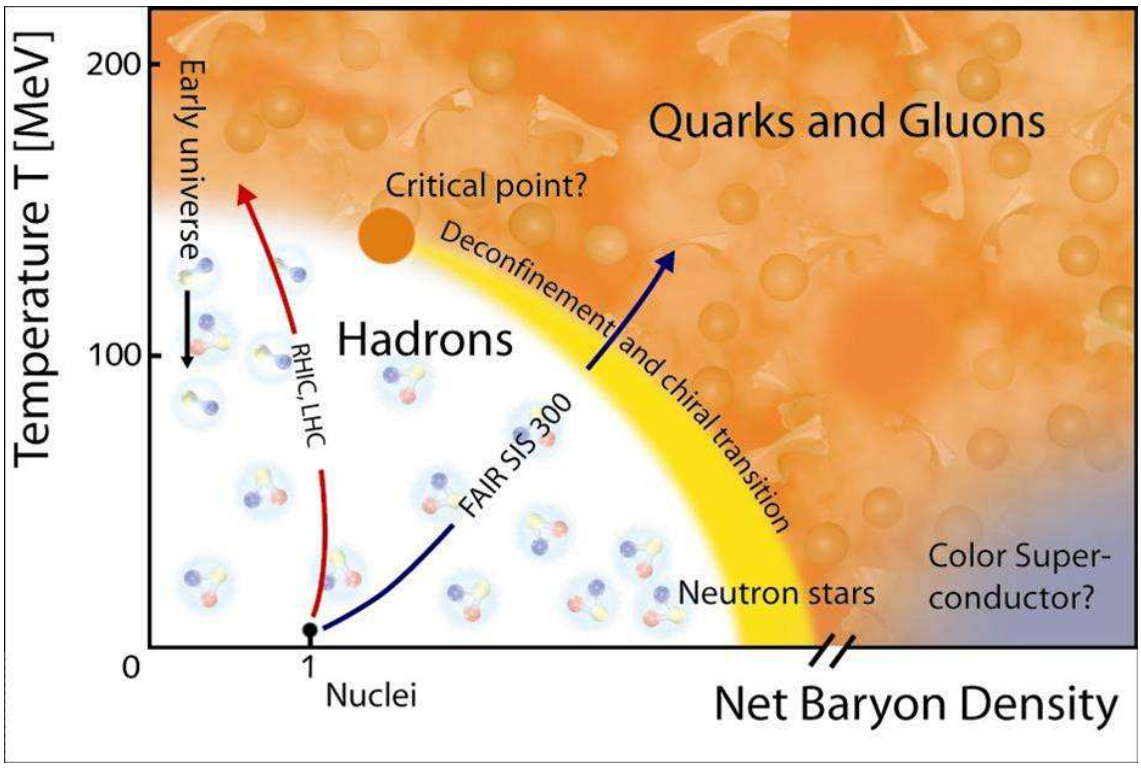

Figure 1.1: The QCD phase diagram. Taken from Ref. [4]

Lattice QCD[1] (lQCD) predicts [5 - 7] a phase transition from hadronic gas (quarks

[1]Lattice QCD is formulated on a space-time discrete lattice and provides the framework for investi-

are bound in hadrons) to a QGP (system of free quarks and gluons) at a critical temperature $T_c \approx 170$ MeV $\approx 10^{12}$ K (at $\mu_b = 0$[2]). The phase diagram is shown in Figure 1.1. The transition temperature corresponds to an energy density $\epsilon \approx 1\text{GeV/fm}^3$, almost an order of magnitude larger than that of normal nuclear matter.

In general, it is believed that the QGP existed in the early stages of our Universe and the QCD phase transition from QGP to hadron gas occured about from 10^{-5} s to 10^{-4} s after the Big Bang. In present day Universe, the QGP is expected to exist in the cores of the neutron stars and/or in more exotic quark stars [8].

1.1 Heavy Ion Collisions

It was proposed that the QGP could be created and studied in laboratory by relativistic heavy ion collisions [9, 10]. Investigations of ion collision started at the Bevalac in Berkeley [11] (1975-1985), and continued at the AGS [12] at BNL (1987-1995), the SPS [13] at CERN (1987-present), the SIS [14] at GSI (1990 - present) the RHIC [15, 16] at BNL (2001 - present). They will be studied at the LHC at CERN [17] (from 2008) and the FAIR at GSI [18] (from 2014).

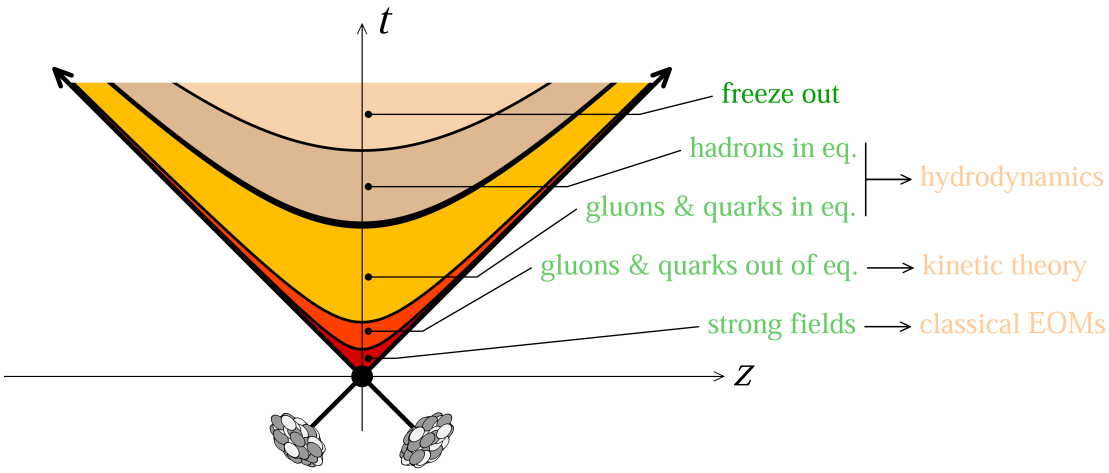

Figure 1.2: The chart of one-dimensional space-time evolution of matter created in heavy ion collision.

The space-time evolution of QCD matter after heavy ion collision can be seen in Figure 1.2. Immediately after collision, quarks and gluons are liberated from nucleons due to the deposited energy and high temperature in collision. After the lapse of 10^{-24} s, quarks and gluons thermalize and QGP is created and it expands. After 10^{-23} s, the phase transition from QGP into hadronic matter occurs and the hadronic gas continues in expansion. Final stage is so-called freeze-out. How the matter expands, the inelasting scattering among hadrons stops. At this point, the

gation of non-perturbative phenomena such as confinement

[2]baryonic chemical potential

species of hadrons do not change anymore. This stage is called chemical freeze out. Eventually also the elastic scattering is over and hadrons further do not interact, this stage is called a kinetic freeze-out. What is observed in the detectors are hadrons emerging from the kinetic freeze-out. Fortunately, the distributions of hadrons to same extend remember the information about QGP formation in the early stages after nuclei collision.

In Ref. [19, 20], several probes were proposed as possible signatures of QGP:

- direct photons [21, 22]
- low-mass dileptons [23]
- strangenes [24]
- charmonium suppression [25, 26]
- jet quenching [27]
- fluctuations [28, 29]

In the next sections, there are described the most important and expected but also some surprising discoveries of heavy ion programme.

1.1.1 SPS era

Several experiments made observations providing evidence that a "new state of matter" was produced in heavy-ion collisions at SPS energies [30]. There was discovered a collective behavior of nucleus-nucleus collisions, futhermore, several unexpected discovers have been reported, such as J/ψ suppression, enhancement of multistrange baryons, low-mass dilepton enhancement which are described in the following section.

COLLECTIVE EXPANSION

HBT[3] [31 - 35] interferometric mesurements of identical particles provide a tool with which we can study the space-time evolution of collision. The interferometric measurement using pions and kaons have been caried out at AGS nnd SPS. From three dimensional analysis of two pions, the transverse radii at midrapidity can be seen to increase with centrality[4] of the collisions: larger radii are observed in larger colision systems. In central Pb+Pb collisions, there was observed that the medium size is about two times larger then the geometrical size of the colliding nuclei. The interferometric radii reflect the later stage of the collision, which is preceded by a large expansion [36 - 38].

[3] Hanbury-Brown and Twiss

[4] Centrality of collision is defined through impact parameter b, where b is the distance of centres of colliding nuclei. The collision is central (centrality = 0%), if $b = 0$, e.g. for centrality 0-100%, b goes from $b_{min} = 0$ to $b_{max} = R_{nucl}$. For instance, centrality 0-20% means 20% of the most central events.

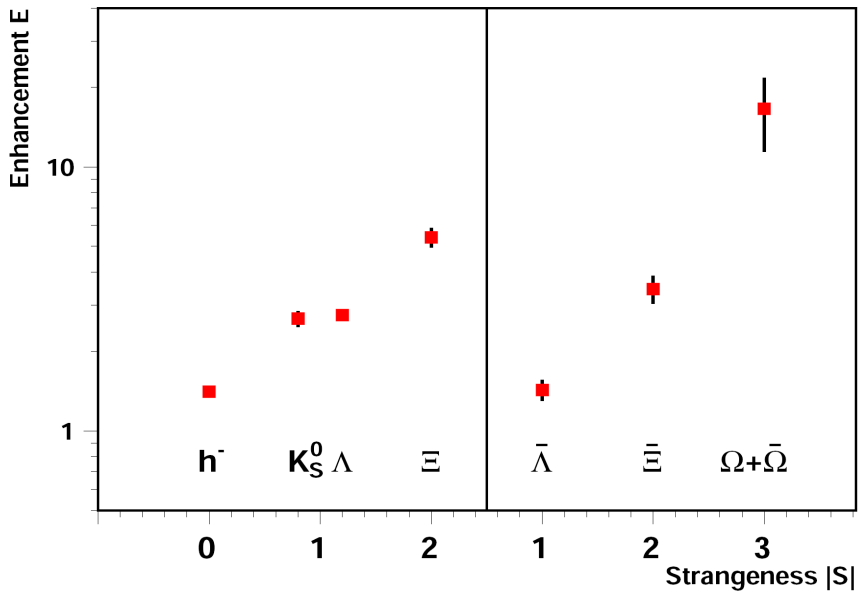

Figure 1.3: The enhancement factor for mid-rapidity yields per participating nucleons in 158 AGeV Pb+Pb relative to p+Pb collisions for strange and non-strange hadrons. Taken from [43]

This results shows that the fireball is in a state od tremendous explosion, with an expansion velocity of half the speed of light and temperature of about 120 MeV. Such an explosion would be driven by strong pressure built up in the early stage of collision.

STRANGENESS

The strangeness enhancement [39, 40] in Pb+Pb collision with comparision with p+Pb was observed at SPS and AGS [41] (see Figure 1.3). The abundance of strange and multistrange particles and their antiparticles suggests the chemical equilibrium. Since they have got small cross sectionw with medium, they can not have enough time to reach equilibrium if they are only produced by parton interaction.

However it is perfectly consistent with a statistical hadronization picture [42], where multi-strange particles profit more from the global strangeness enhancement than singly strange hadrons.

LOW-MASS DILEPTON ENHANCEMENT

The CERES experiment [44] measured low-mass electron-positron pairs in p+Be, p+Au and Pb+Au collision. In the p+Be and p+Au [45, 46], exclusive π^0 and η measurements was carried out and then compared with production of inclusive electron-positron pairs. It was shown that the observed spectra corresponds to the direct vector meson decays and π^0 and η Dalitz decays (see Figure 1.4). The relative

meson abundances of these meson in p+Be and p+Au collision looks to be the same. However, in Pb+Au. there is seen significant excess in the region below the peak of ρ meson (see Figure 1.5).

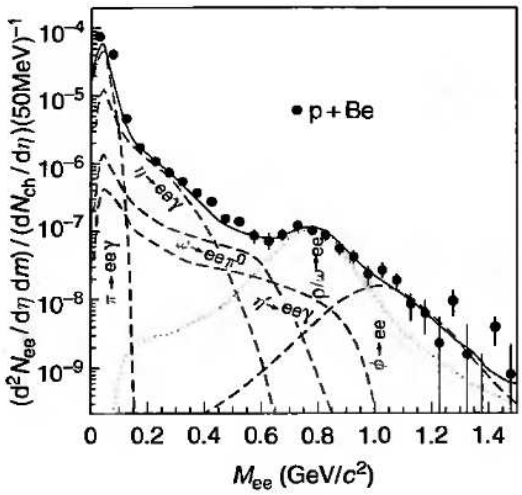

Figure 1.4: Inclusive invariant electron-positron spectrum observed in p+Be collisions. The solid line shows electron-positron yield from hadronic decays. The contributions of particular decays are shown as dashed lines. Taken from ref. [45]

J/ψ SUPPRESSION

At SPS, there was observed the suppresion of J/ψ production yield [47, 48] in comparison with the ordinary nuclear absorption (in central Pb+Pb collision about 70% [49]). The formation of QGP would have the effect of screening the color binding potential [26], preventing the c and $\bar{c}$ quarks from forming of charmonium state.

m_T SCALING

Single particle spectra (or invariant cross-sections) plotted as a function of $m_T - m$ (see Figure 1.7) can be described by exponential decreasing function, except for low-m_T[5] region of pions. A steeper component of the π's for $m_T - m < 0{,}2$ GeV contains contributions from the decay of the (mainly Δ) resonances. The distributions are restricted to $m_T - m < 1$ GeV due to experimental limitations of particle identification.

To compare their slopes, the distributions are fitted to the function $exp(-\frac{m_T}{T})$, where T is the inverse slope parameter.

The inverse slope parameter is proportional to the mass of the particles [51, 52], and this effect becomes larger in heavy nuclei collisions (e.g. Pb+Pb) than light ones

[5] $m_T = \sqrt{m^2 + p_T^2}$, where m is particle rest mass, and p_T is transverese momentum, $\vec{p_T} = \vec{p_x} + \vec{p_y}$, where xy-plane is perpendicular to beam axis.

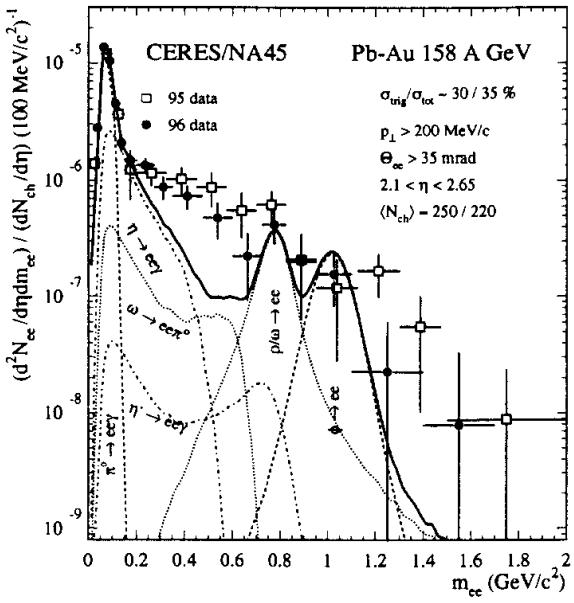

Figure 1.5: Inclusive invariant electron-positron spectrum observed in Pb+Au collisions. The solid line shows electron-positron yield from hadronic decays. The contributions of particular decays are shown as dashed lines. Taken from ref. [46]

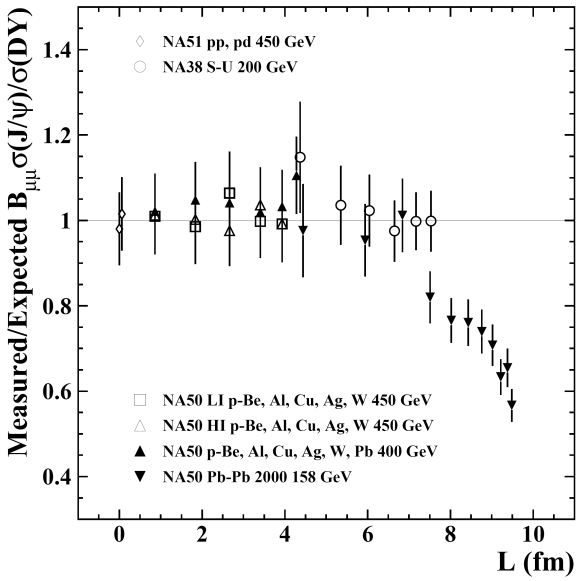

Figure 1.6: Measured J/ψ production yields, normalised to the yields expected assuming that the only source of suppression is the ordinary absorption by the nuclear medium. The data is shown as a function of the energy density reached in the several collision systems. Taken from ref. [50].

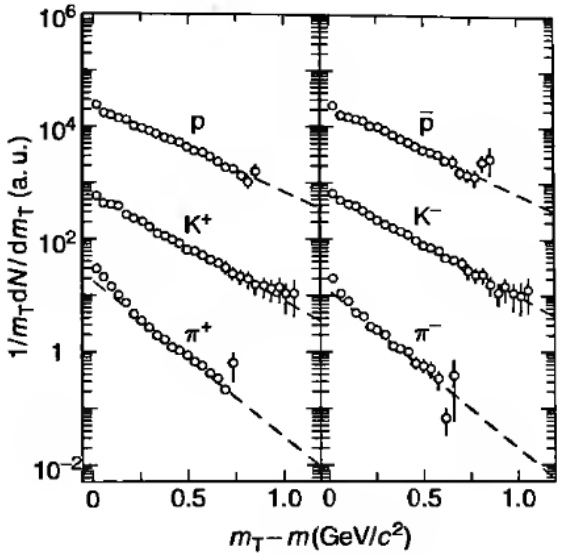

Figure 1.7: m_T spectra of various particles. Taken from ref. [51]

(e.g. S+S). The T parameter for pions is similar to those for both pp collisions and AA collisions, the slopes of heavier particles become flatter in AA than in pp collisions. The mass dependence of the slope parameter provides evidence of collective transverse flow from expansion of the system in heavy ion central collisions.

1.1.2 RHIC Era

This section alludes to main, up to now, discoveries at RHIC such that elliptic flow, high p_T-particle suppression, perfect liquid behavior of created nuclear matter. Summary and critical overview of first 5 years of RHIC programme has been reported by each experiment in [53].

ELLIPTIC FLOW

One of the first observables measured at RHIC was the so called elliptic flow [54]. Any strong scattering in early stage after collision converts the spatial anisotropy (Figure 1.8) to a momentum anisotropy of particles which are emitted from non-central heavy-ion collisions. Elliptic flow is characterized by the second harmonic coefficient $v_2(y, p_T)$[6] of an azimuthal Fourier decomposition of the momentum distribution [55, 56].

Elliptic flow is a self-limiting phenomenon, which is readily understood in the thermodynamic limit. If strong scattering is sufficient to establish local thermal equi-

[6] $E\frac{d^3N}{d^3p} = \frac{1}{2\pi p_T}\frac{d^2N}{dp_T dy}\left(1 + \sum_{n=1}^{\infty} 2v_n cos\left[n(\phi - \Phi_R)\right]\right)$, where v_n is n-th component of Fourier expansion, ϕ is particle track azimuthal angle, Φ_R is the azimuthal angle of the reaction plane in the laboratory frame, and $y = \frac{1}{2}log\frac{E+p_z}{E-p_z}$ is rapidity.

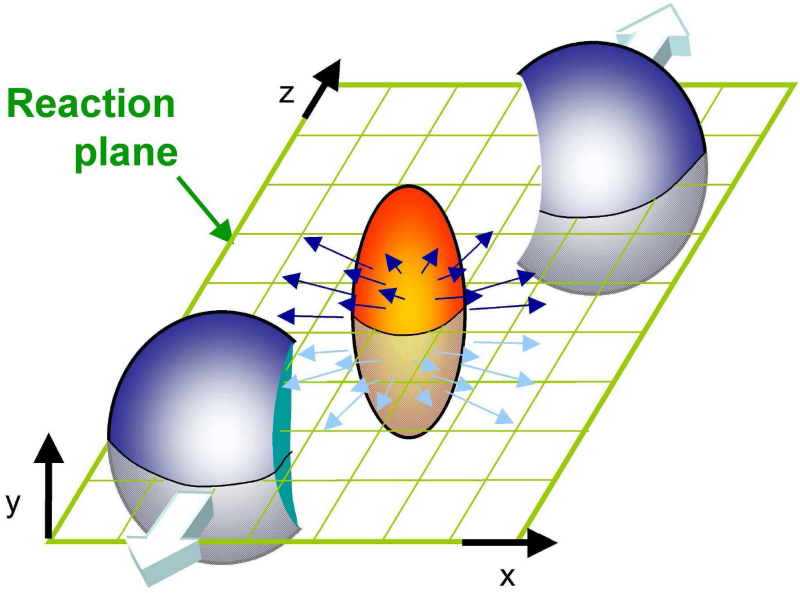

Figure 1.8: Spatial asymmetry with respect to the reaction plane of the produced "fireball" in non-central nucleus-nucleus collisions

librium, then the pressure gradient is largest in the shortest direction of the ellipsoid. This produces higher momenta in that direction, quickly reducing the spatial asymmetry.

Elliptic flow is especially sensitive to the early stages of system evolution [57, 58]. A measurement of v_2 thus provides access to the fundamental thermalization time scale in the early stages of a relativistic heavy-ion collision [59, 60].

Figure 1.9 shows the collective flow at baryon and meson level and Figure 1.10 show the collective behavior at quark level. The elliptic flow of charged particles (π, K, p, Λ) at RHIC is well described by a hydrodynamical model up to p_T ~1,2 GeV [62]. The agreement of measured data and this model is shown in Figure 1.11. The hydrodynamic models assume the nuclear matter is a perfect liquid with zero viscosity.

HIGH p_T SUPPRESSION

At RHIC was observed the suppression of production of hadrons with high-p_T (5 - 10 GeV) in central Au+Au collisions as compared to scaled production from p+p collisions [63 - 66]. This is related to energy loss of ligh partons in created dense nuclear matter. The suppression is characterized by nuclear modification factor R_{AA}[7]. In the absence of medium effects, the nuclear collisions can be viewedat high p_T as a superposition of elementary hard nucleon-nucleon collisions. Consequently we

[7]The nuclear modification factor is obtained from the particle p_T distributions in A+A collisions ($d^2N_{AA}/dp_T dy$) and in p+p collisions ($d^2N_{pp}/dp_T dy$) as: $R_{AA} = \frac{d^2N_{AA}/dp_T dy}{\langle N_{coll}\rangle d^2N_{pp}/dp_T dy}$, where $\langle N_{coll}\rangle$ is the average number of nucleon-nucleon collisions corresponding to a given centrality.

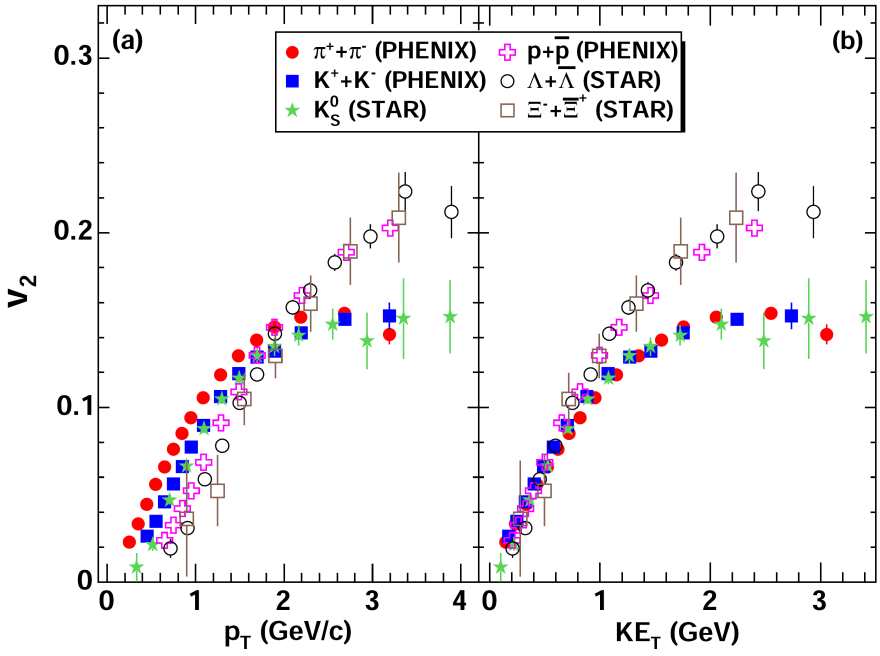

Figure 1.9: (a) v_2 vs p_T and (b) v_2 vs KE_T for identified particle species obtained in minimum bias Au+Au collisions. Taken from [61]

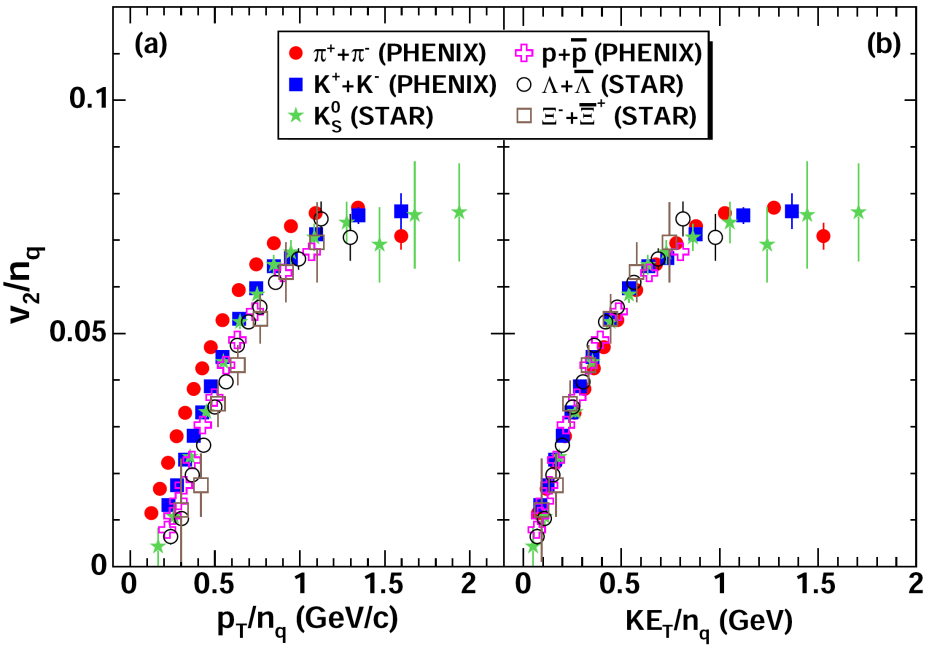

Figure 1.10: (a) v_2/n_q vs p_T/n_q and (b) v_2/n_q vs KE_T/n_q for identified particle species obtained in minimum bias Au+Au collisions. Taken from [61]

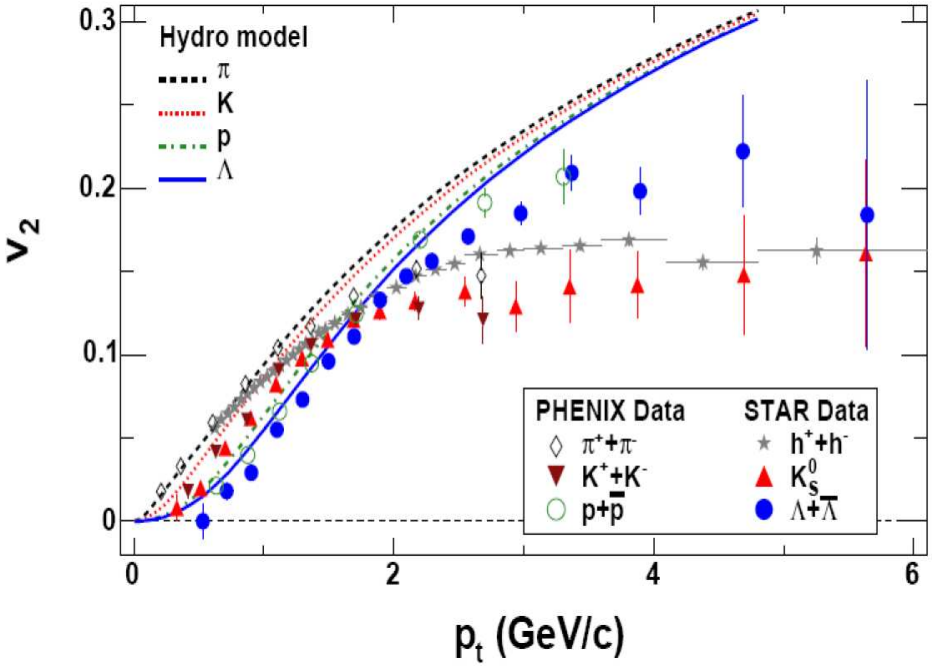

Figure 1.11: Comparison od particle elliptic flow v_2 with hydrodynamical model. Taken from [62]

expect $R_{AA} \sim 1$ at high p_T (see Figure 1.12). For $p_T < 2$, where the particle production is scaled by the number of participants of collision, R_{AA} is less than one. In fact, it is found that $R_{AA} > 1$ for $p_T > 2$ GeV in nuclear reactions at lower energy. This enhancement, first observed by Cronin, is associated with multiple scattering of partons [67, 68] in nuclear matter.

Surprisingly, $R_{AA} < 1$ at high p_T for central collisions was observed at RHIC (see Figure 1.13), while $R_{AA} \sim 1$ for more peripheral collisions. The observed suppression is of factor of ~ 5 for $p_T > 6$ GeV.

Energetic partons propagating through a dense medium are predicted to lose energy [69 - 77] thus producing a suppression in the yield of high-p_T hadrons produced from the fragmentation of these partons. Au+Au measurements at RHIC [64 - 66, 78 - 80] demonstrated such a suppression. The results of d+Au measurements [86 - 89] showed that the suppression was not due to initial-state effects (see upper point in Figure 1.13).

The suppression of the yield of high-p_T hadrons is generally believed to provide a direct experimental probe of the density of color charges in the medium through which the parton passes [81 - 83]. The observed suppression of high-p_T particle production at RHIC is a unique phenomenon that has not been previously observed in any hadronic or heavy ion collisions at any energy. The suppression provides direct evidence that Au+Au collisions at RHIC have produced matter at extreme densities, greater than ten times the energy density of normal nuclear matter and the highest energy densities ever achieved in the laboratory. Medium-induced energy loss, pre-

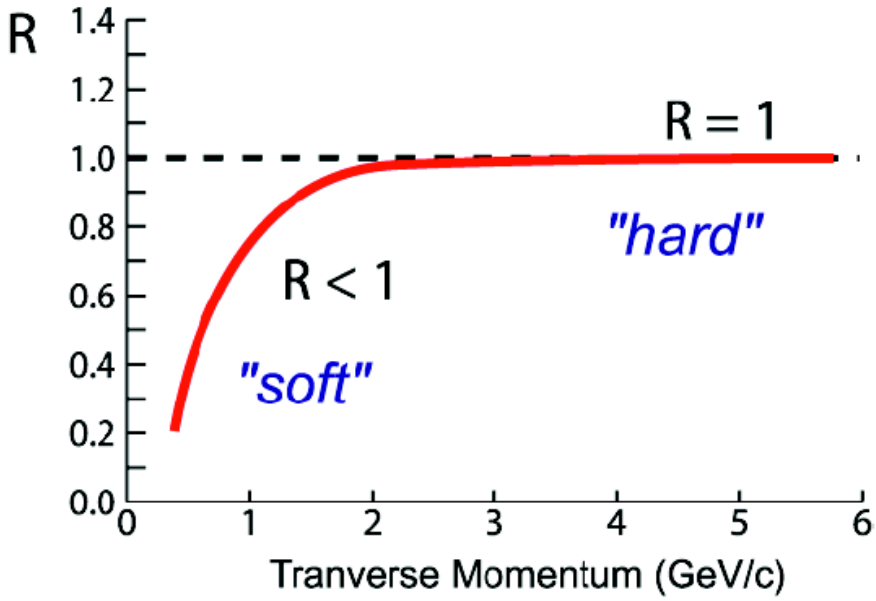

Figure 1.12: Chart of expected trend of R_{AA} without nuclear effect. At low p_T, R_{AA} is less than one because particle production is scaled by number of colliding nucleons. At high p_T, the binary collisions are expected therefore R_{AA} should be equal to one.

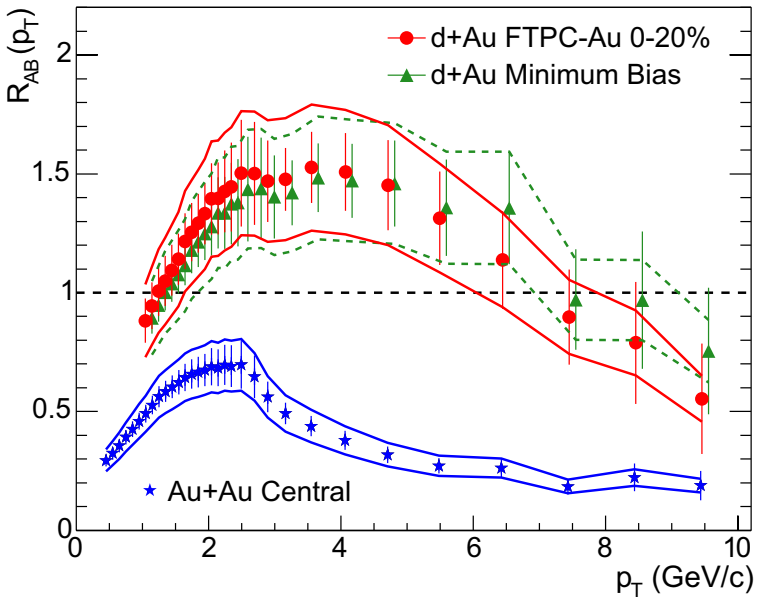

Figure 1.13: Binary-scaled ratio R_{AB} of hadron inclusive yields from 200 GeV Au+Au and d+Au relative to that from p+p collisions, from STAR [53].

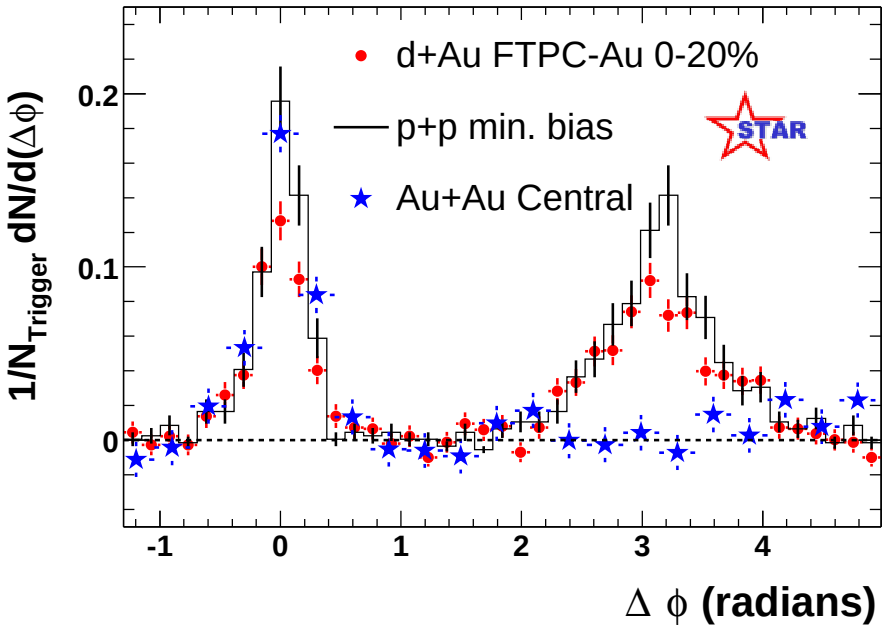

Figure 1.14: Two particle azimuthal correlations of high p_T hadrons. Taken from [53].

dominantly via gluon bremsstrahlung emission [84, 85], is the only currently known physical mechanism that can fully explain the magnitude and p_T dependence of the observed high-pT suppression.

HIGH p_T SUPPRESSION OF AWAY SIDE PEAK

Direct reconstruction of jets in nuclear collisions is currently impossible due to the presence of the large background of soft partons. Nevertheless STAR [90, 91] and PHENIX [92, 93] have directly observed the presence of jets by studying two particle azimuthal correlations[8](e.g. for Figure 1.14 $p_T^{trigg} > 4$ GeV and $2 < p_T^{assoc} < p_T^{trigg}$). The peaks observed at $\Delta\phi = 0$ ("near side peak") reflect the correlation between particles which are produced within the same jet while usualy the broader peaks observed at $\Delta\phi = \pi$("away side peak") reflect the correlations between hadrons produced in oposite direction jet. In the Au+Au collision, the jet angular correlations are modulated by the elliptic flow of particles in the combinatoric background. However, this contribution has got only little effect on the shape of near-side peak in the $\Delta\phi$ distribution. The azimuthal correlations were performed for both p+p collisions and Au+Au collisions but also for d+Au collisions used as benchmark of initial state [90, 91, 94]. The near-side peak is similar in all three systems [91] that is typical of jet production, and a back-to-back ($\Delta\phi = \pi$) peak similar to that seen in p+p and peripheral Au+Au collisions [91]. This is typical of di-jet events.

However, the back-to-back peak in central Au+Au[6] shows a dramatic suppression relative to p+p and d+Au or peripheral Au+Au (see Figure 1.14). The contrast

[8]For more details of azimuthal correlation techniques see Appendix A.

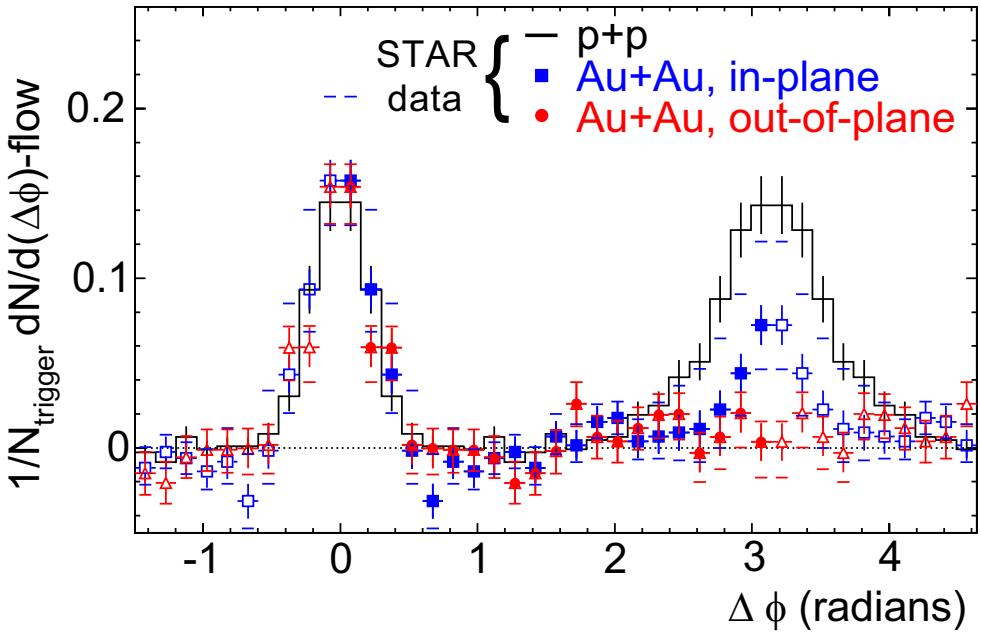

Figure 1.15: Correlations for different orientation of the trigger hadron in relation to collision reaction plane. Taken from [53].

between d+Au and central Au+Au collisions indicates that the strong high p_T suppression is observed and is associated with the produced medium in Au+Au but not in d+Au collisions. This means that in the central collision the backward jet was quenched in the dense medium and this phenomenon is known as jet quenching.

General interpretation of these results is that, in the final state following the hard scattering, energetic partons traverse the dense medium in the central region of the collision lose energy, and the observed jets, primarily, comes from partons produced near the surface and directed outwards [91].

In non-central collisions, the suppression should depend on the relative orientation of the back-to-back pair with respect to the reaction plane [95] (see Figure 1.15). In the region around $\Delta\phi = \pi$, we observe an excess for the inplane distribution, but no excess is found for the out-of-plane distribution. the path length in medium for a dijet oriented out of the reaction plane is longer than in the reaction plane, leading to correspondingly larger energy loss.

SOFT p_T STRUCTURE OF AWAY SIDE PEAK

In jet quenching the energy of away side jet did not disappear and is distributed to particles with smaller momentum. In order to study such particles and correlation function, the soft p_T ($1,0 < p_T^{assoc} < 2,5$ GeV and $2,5 < p_T^{trig} < 4,0$ GeV)hadrons have to be measured.

MACH CONE Correlation data with lower p_T-threshold for associated particles show a broader peak or even a double-peaked structure in the backward region [96

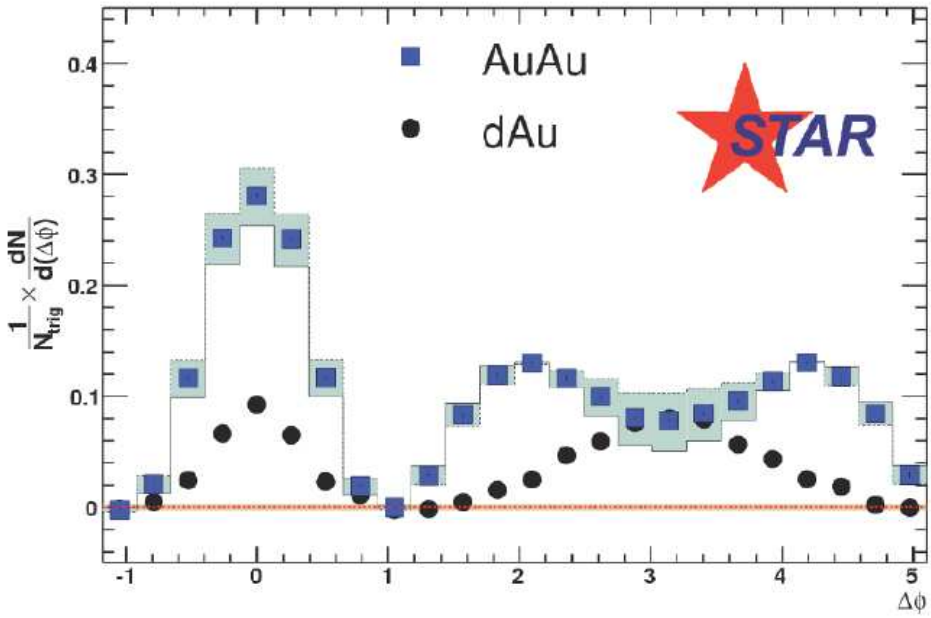

Figure 1.16: Azimuthal distributions for $1,0 < p_T^{assoc} < 2,5$ GeV and $2,5 < p_T^{trig} < 4,0$ GeV shown the double hump structure in central Au+Au collisions (blue). d+Au results (black) are shown for reference. Taken from [103]

- 102] (see Figure 1.16).

The experimental azimuthal dihadron distributions at RHIC show a double peak structure in the away side ($\Delta\phi = \pi \pm 1{,}2$ rad) for intermediate pt particles. A variety of models have appeared trying to describe this modification.

The observed shape could be a consequence of the emission of sound by a supersonic high momentum particle propagating in the hot dense medium. The hydrodynamical behavior of the medium leads to collective effects, for example, to the formation of a Mach Cone [105 - 107] (see Figure 1.17).

The redistribution of the jet energy and momentum is reflected in the correlations of particles associated with the jet. In fact, the experimental dihadron correlation function shows, at intermediate pt, a double peak structure in the away side with the maximum of the correlation at $\Delta\phi = \pi \pm 1{,}2$ rad. [108, 109]. The study of three particle correlations also indicates that the structure responsible for this modification is conical [104].

The interference of sound waves from a supersonic source leads to the Mach Cone, a conical flow directed at an angle from the jet $cos\theta_M = c_s$

The medium expansion also affects the direction of propagation of the shock. As the RHIC fireball cools down the speed of sound of matter changes from $c_s^2 = 1/3$ in the QGP phase to $c_s = 0$ in the mixed phase and to $c_s^2 = 0{,}2$ in the hadron gas [110, 111].

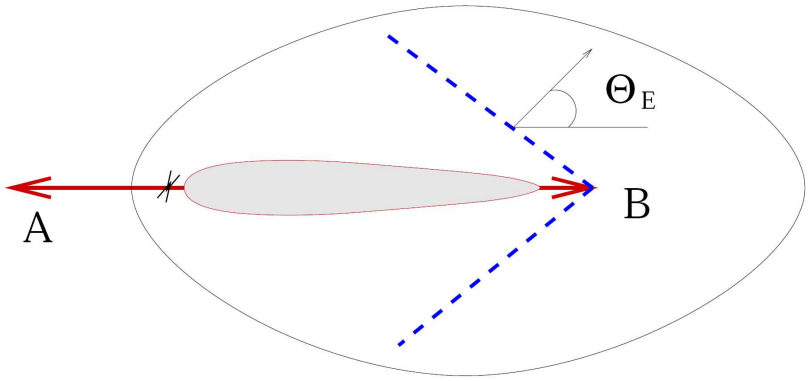

Figure 1.17: A schematic picture of the origin of the Mach cone and the double hump structure in away side peak. The trigger jet (A) travels a short distance in the medium while the backward jet (B) propagates though the entire medium. When it travels by supersonic velocity, the Mach shock wave is created and the shock wave interaction with the medium leads to emission of particles at an angle $\theta_E = 1{,}2$ rad from the backward jet axis. A similar picture describes the Cherenkov and large angle gluon radiation scenarios. Taken from ref. [104]

CHERENKOV CONE The same angular pattern, like for Mach cone, could also be a result of Cherenkov gluon radiation [112 - 114]. Cherenkov and Mach waves have got different physical principles. However, it is not easy to reveal this feature in experiment. Their common feature is the radiation cone. Cherenkov radiation must result in two humps of the one-dimensional pseudorapidity distribution and in ring-like structure of two-dimensional plots. They have been observed.

Pure Cherenkov radiation leads to energy loss which, however, is too small to account for the jet suppression observed in RHIC experiments. On the other hand, collision-induced Cherenkov-like bremsstrahlung [115] can explain both the observed energy loss and the emission pattern of soft hadrons in the direction of quenched jets.

DEFLECTED JETS All the previous scenarios are characterized by conical emission of particles in around the axis of jet. However, some authors have proposed mechanisms in which the away side peak structure observed in the azimuthal correlations is due to a shift of the entire jet to a finite angle off the jet axis.

However, the scenarios based on jet deflection [116, 117] seem disfavored by the recent Mach Cones in QGP results on three particle correlations [104].

RIDGE

The observed $\Delta\eta$-$\Delta\phi$ correlation [118 - 123] of particles reveals the new surprising feature known as ridge (see Figure 1.18). There are particles associated with the

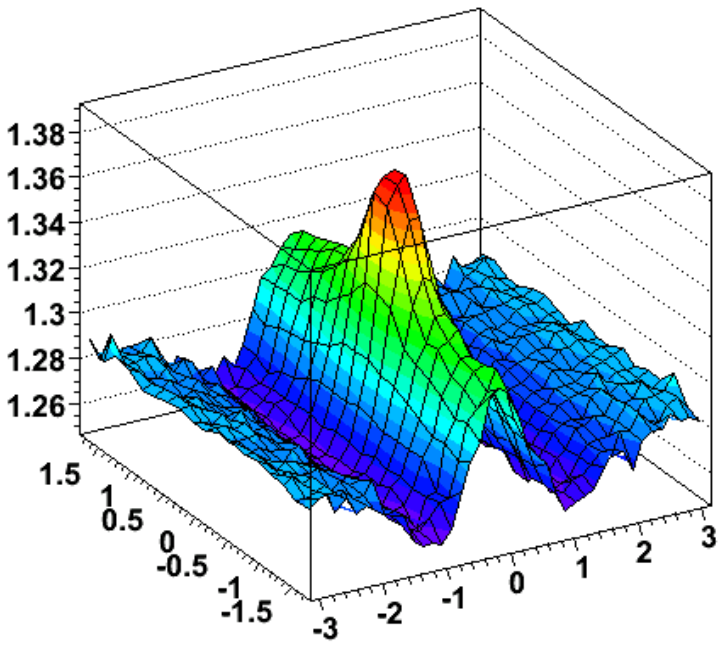

Figure 1.18: The $\Delta\phi \times \Delta\eta$ dihadron correlation function in central Au+Au collisions for $3 < p_T^{trig} < 4$ GeV and $p_T^{trig} > p_T^{assoc} > 2$ GeV. Taken from ref. [120]

trigger jet within a small cone of ($\Delta\eta$,$\Delta\phi$) $\sim$ (0, 0) which belong to the remnants of the near-side jet component. In addition, there are particles associated with the trigger jet within a small range of $\Delta\phi$ around $\Delta\phi = 0$ but distributed broadly in $\Delta\eta$.

While many theoretical models have been proposed to discuss the jet structure and related phenomena [117, 124 - 129], the ridge phenomenon has not yet been fully understood.

1.1.3 Future Heavy Ion Program

In the near future, the LHC [130] at CERN will start with p+p and/or Pb+Pb collisions at 5,5 ATeV (Pb+Pb)and 14 TeV (p+p). There will be three experiments capable to investigate heavy ion collisions - ALICE [131], ATLAS [132], and CMS [133]. The detector ALICE is directly dedicated for research to hot dense nuclear matter or even QGP. One is believing that, at LHC, there will be discovered the weakly interacting and long lived QGP, started b quark and W and Z bosons production in QGP.

Nowadays also the upgrades of RHIC are planed. The first upgrade is RHIC-II [134] (2012) with beam cooling (probably stochastic) for reaching higher luminosity. Both STAR and PHENIX will be upgraded, too. Vertex detectors will be installed inside both ones: Heavy Flavor Tracker [135], for STAR, and Silicon Ver-

tex Tracker [136], for PHENIX. The second upgrade of RHIC called eRHIC [134] is electron-heavy ion collider dedicated for research of pre-initial collision state is also proposed.

Another experiment in preparation is the CBM (Compressed Baryon Matter) at FAIR at GSI [137]with U+U collisions. This fixed target experiment will invesigate another region of QCD phase diagram in the baryon rich region (see Fig. 1.1). The FAIR facility is expected to come operation in 2014.

Chapter 2

Heavy Quarks

Heavy quarks can be produced by quark antiquark interaction forming a virtual gluon that is then decaying into $c\bar{c}$ (charm) or $b\bar{b}$ (beauty/bottom) pair. However, the most important production mechanism of these quarks is gluon fusion [138, 139]. Because of their large masses, their production can be calculated by pQCD [140] and also one expects that their thermalization time is much longer than for light quarks. Since heavy quarks are primarily produced during early stages of a collision of nuclei and then they interact with the medium, they can be used as a probe of space-time evolution of the medium arising from heavy ion collision.

The study of heavy flavors in relativistic nuclear collisions follows two different approaches:

- direct reconstruction of heavy flavor mesons,
- identification of electrons and muons from semileptonic decays (see Figure 2.1) of open charm mesons (that is such that contain one heavy and one light quark).

Direct reconstruction of heavy flavor mesons is being performed by STAR using the decay chanell $D^0 \rightarrow K^-\pi^+$ (BR = 3,83 %) in d+Au and Au+Au collisions [141].

The use of semileptonic decays of open heavy flavor mesons (e.g. $D^0 \rightarrow e^+K^-\nu_e$) over broad p_T range, provide more efficient measurement of charm and bottom production. The major dificulty in the electron analysis is the fact that there are many sources of electrons other than semileptonic decays of heavy flavor mesons, for instance photon conversion of decaying light mesons.

Theoretical models predicted that heavy quarks have smaller energy loss than light quarks when they propagate through hot nuclear matter due to the suppression of gluon radiation into small angles (”dead cone” effect [142]).

However, RHIC data for electron spectra from semileptonic decays of heavy quarks (charm) in Au+Au collisions show a strong suppression ($R_{AA} \approx 0,2 - 0,3$ - similar to light hadrons - see Figure 2.2). Moreover nonzero elliptic flow (about 10%) was observed [143 - 150]. This is indicating substantial collective behavior and thermalization of charm quarks in the expanding fireball.

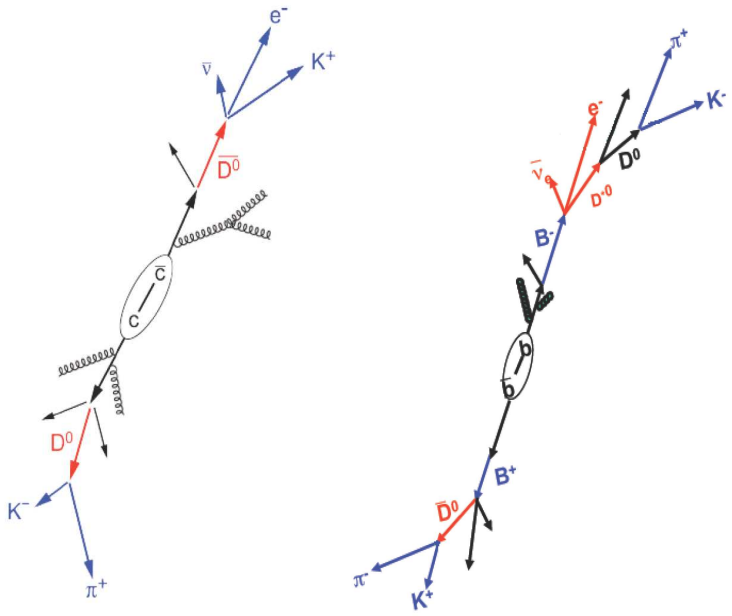

Figure 2.1: **Left:**The chart of c quark (D^0 meson) decay kinematics. **Right:** The chart of b quark (B^0 meson) decay kinematics.

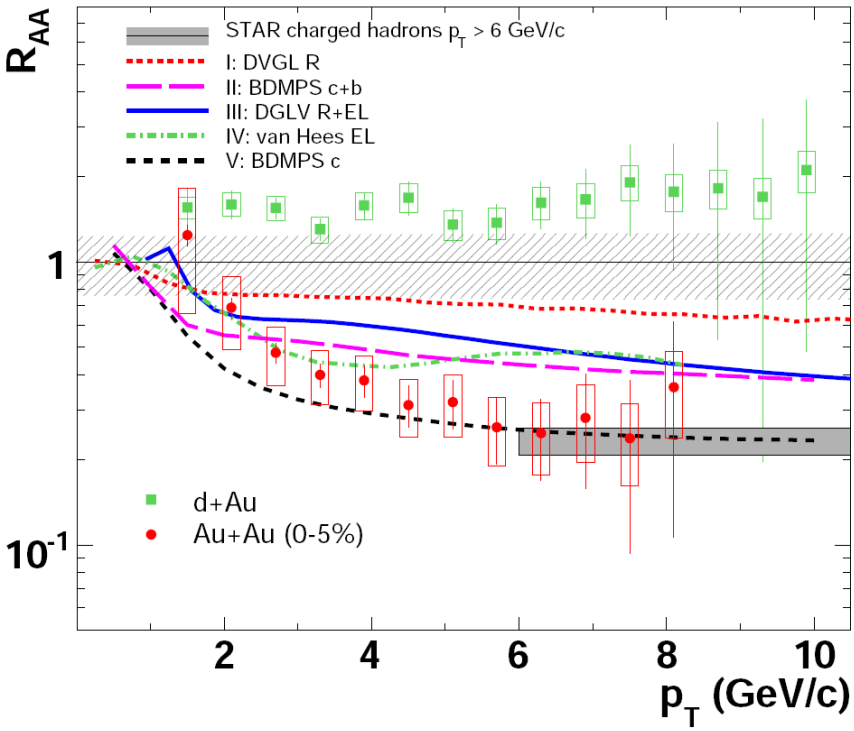

Figure 2.2: The non-photonic electron suppression in central Au+Au collisions compared with models of interactions of heavy quark. Taken from ref. [53]

In Ref. [151, 152], there is suggested that one of the basic assumptions of models is the fact that the collisional energy loss is negligible compared to radiative [153], is probably incorrect and for a several parameters relevant for RHIC, radiative and collisional energy losses for heavy quarks are comparable. Therefore collisional energy loss can not be neglected in the computations of jet quenching mechanism. However even after inclusion of collisional energy loss the heavy flavor suppression in the medium cannot be explained. Theoretical attempts to explain the non-photonic electron suppression are not yet succesfull.

Chapter 3

RHIC Facility and Detector STAR

3.1 RHIC

The Relativistic Heavy Ion Collider (RHIC) is located at Brookhaven National Laboratory. The whole RHIC complex is shown in Figure 3.1. Heavy ions started their acceleration in the Tandem Van de Graaff that accelerates ions at about 5% the speed of light (1 AMeV). There is gold foil that stripes electrons. Then only +32 charged gold ions are selected and feed them to the Booster. The Booster synchrotron is a small circular radio frakvency accelerator. It accelerates these gold ions to about 37% the speed of light (95 AMeV). At the end of the Booster, there is another gold foil where other electrons are stripped. The +77 charged gold ions are sent into the Alternating Gradient Synchrotron (AGS) to be accelerated further up to around 99,7% the speed of light (10,8 AGeV). At the end of AGS, there is the last foil to strip the last two electrons off each gold ion and makes it +79 charged. After this, the gold ions are going toward the AGS-To-RHIC (ATR) transfer line. At the end of this line, there is a switching magnet sending the ion bunches down to one of the two beam lines in RHIC. RHIC can accelerate these ions up to 100 AGeV and collide them in any of the six intersection points on RHIC ring.

In four intersection points, there are located the detectors - two large (STAR [155] and PHENIX [156]) and two smaller ones (BRAHMS [157] and PHOBOS [158]). The STAR detector utilizes a solenoidal geometry with a large cylindrical Time-Projection Chamber (TPC) as a main tracking detector. The PHENIX detector consists of three magnetic spectrometers - one Central Spectrometer with an axial magnet field and two detector arms, and two Muon Arms located in forward and backward direction along the beam axis. The PHOBOS detector consists of a two arm magnetic spectrometer as its central detector and a series of ring multiplicity detectors that are located around beam pipe. The BRAHMS detector consists of a two arm magnetic spectrometer, one in forward direction for measurement of high momentum particles but with a small solid angle and the other on the side of collision point for mid-rapidity region. PHOBOS and BRAHMS have recently finished data taking.

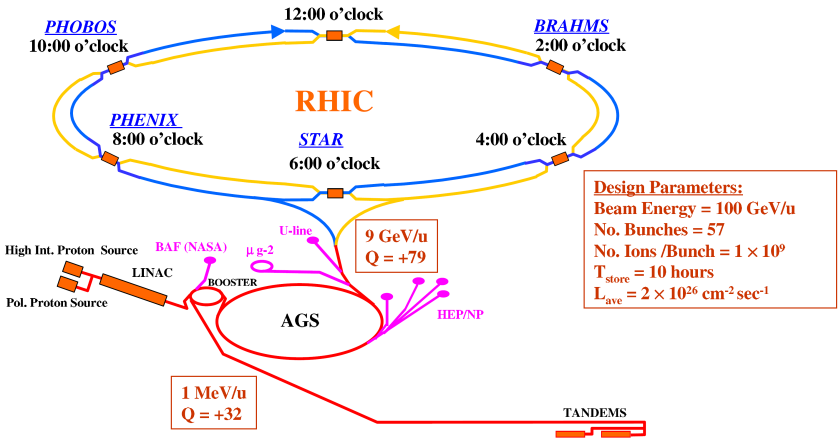

Figure 3.1: RHIC overview illustration. Taken from ref. [154]

3.2 STAR

The Solenoidal Tracker at RHIC (STAR) (see Figure 3.2 and Figure 3.3) is large detector at RHIC. STAR [159] was primarily designed for measurements of hadron production over a large solid angle, and for high precision tracking, momentum analysis, and particle identification at the center of mass rapidity.

A solenoidal magnet [160] with a uniform magnetic field of maximum value 0,5 T allows the analysis of momentum of charged particle.

The main part of STAR detector is Time Projection Chamber (TPC) [**?**, 162] as main tracking system for charged particle tracking and their identification. Around TPC, the Barell Electromagnetic Calorimeter [163] with the Shower Maximum Detector (SMD) is located.

Other detectors are the Forward TPC [164] for extending the tracking to forward region ($2,5 < |\eta| < 4,0$), Endcap Electromagnetic Calorimeter (EEMC)[165], Time Of Flight (TOF) detector [166], and Photon Multiplicity Detector (PMD) [167]. The fast detectors that provide input to the trigger system are a Central Trigger Barrel (CTB) surrounding the TPC at $|\eta| < 1$ and Zerodegree Calorimeters (ZDC) [168] which covers $1 < |\eta| < 2$. Both detectors are used for centrality measurement. And the ZDCs are used for determining the energy of particles going in the forward directions.

Inside the TPC was located Silicon Vertex Tracker (SVT) [169]. In the future, the Heavy Flavor Tracker [135] will be installed closest to the interaction point

3.2.1 TPC

STAR [159 - 171] uses the TPC (see Figure 3.4) as its primary tracking device [162 - 172]. The TPC measures 4m in diameter by 4,2 m long. It cover 2π in azimuthal angle and from -1,8 to 1,8 in pseudo-rapidity. It can record the tracks of particles,

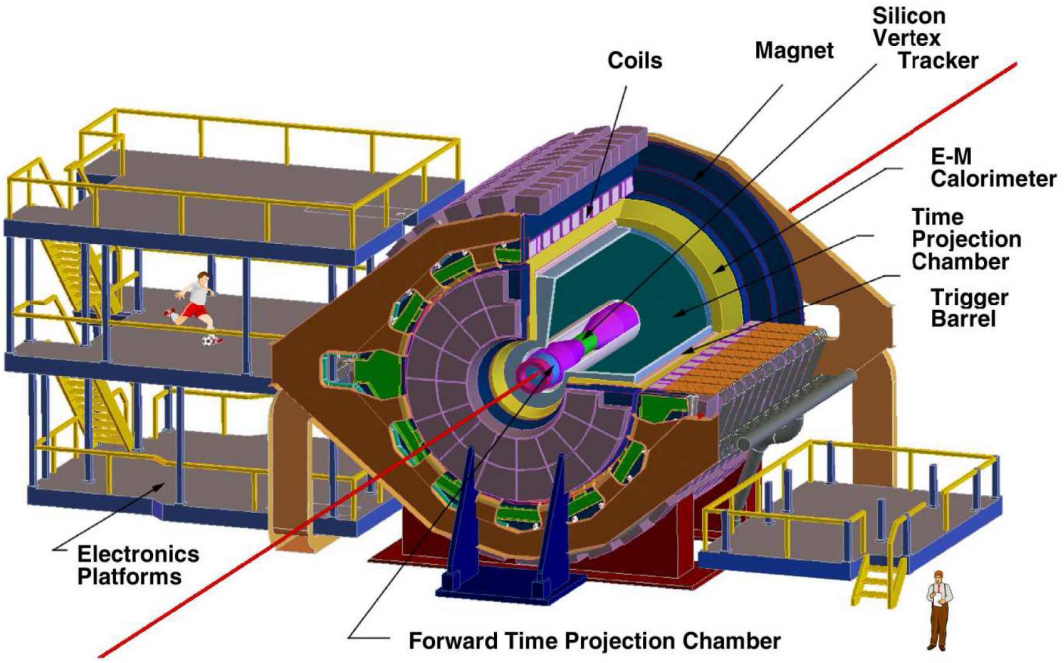

Figure 3.2: STAR detector overview. Taken from Ref. [155]

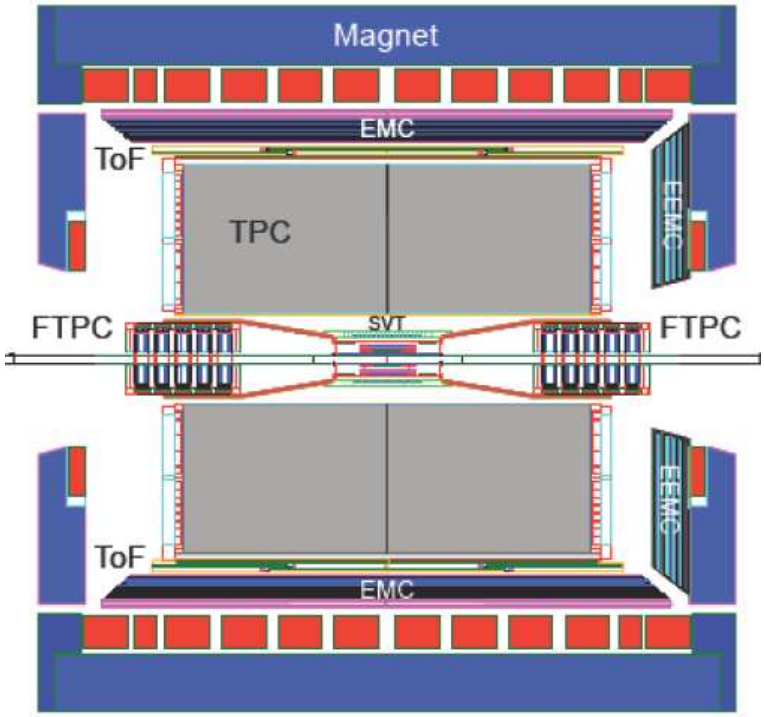

Figure 3.3: Side view of STAR detector. Taken from Ref. [155]

measure their momenta, and identify the particles by measuring their ionization energy loss (dE/dx). Particles are identified over a momentum range from 100 MeV to greater than 1 GeV, and particles momenta are measured over a range of 100 MeV to 30 GeV. The TPC is set in a solenoidal magnet field of 0,5 T [173].

TPC's central membrane is operated at 28 kV. The end caps are at ground, they are divided on the 12 readout sectors. The readout system is based on Multi-Wire Proportional Chambers (MWPC) with readout pads. The track of an infinite-momentum particle passing through the TPC at mid-rapidity would be sampled by 45 pad rows, but a finite momentum track may not cross all 45 rows. The tracks are reconstructed from the pad signals (x, y coordinates) and z coordinate from the electron drift time. The dE/dx is extracted from the energy loss measured on up to 45 pad rows.

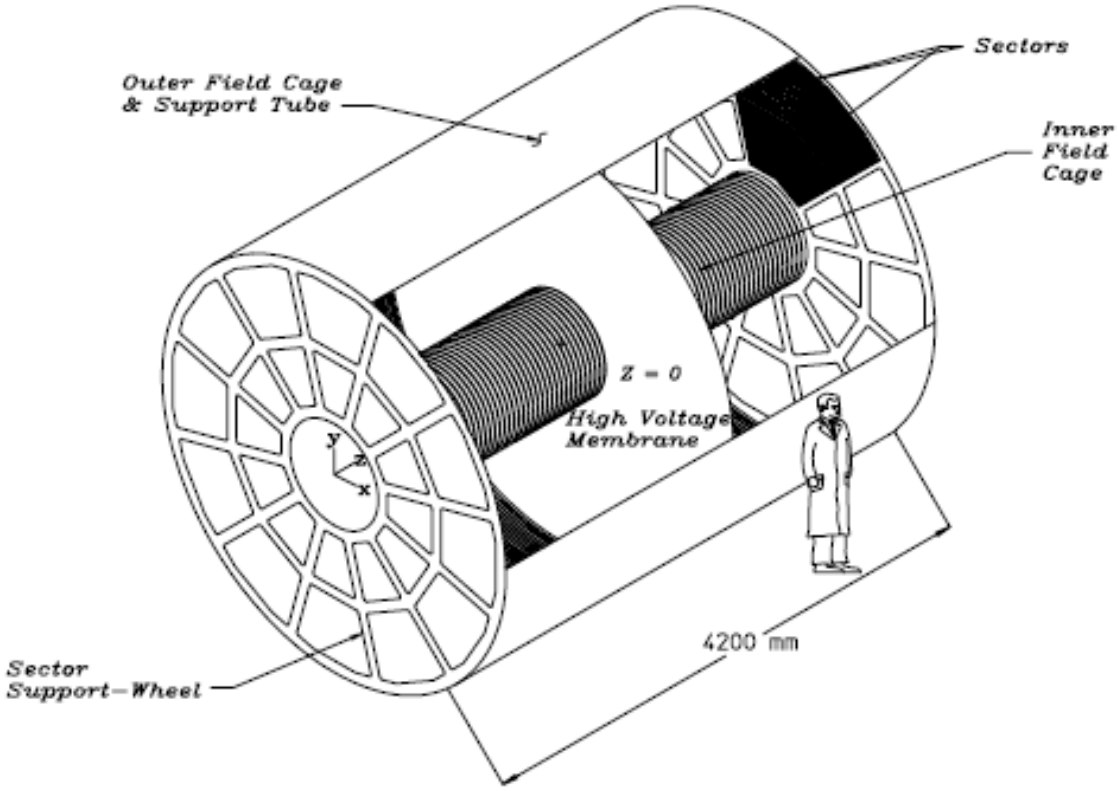

Figure 3.4: Schematic illustration od STAR TPC. Taken from [161].

The x and y coordinates of a cluster are determined by the charge measured on neighbouring pads in a single pad row. The z coordinate of a point inside the TPC is determined by measuring the time of drift of a cluster of secondary electrons from the point of origin to the anodes on the endcap and dividing by the average drift velocity.

3.2.2 BEMC

The barrel electromagnetic calorimeter (BEMC) (see Figure 3.5) allows the reconstruction of the π^0 and isolated (mainly direct) photons and is also able of identifying single electrons and electron-positron pairs against large hadron background. The BEMC covers $-1,0 < \eta < 1,0$ and 2π in azimuthal angle. The inner surface of the BEMC has a radius of about 220cm and the outer radius is about 250 cm.

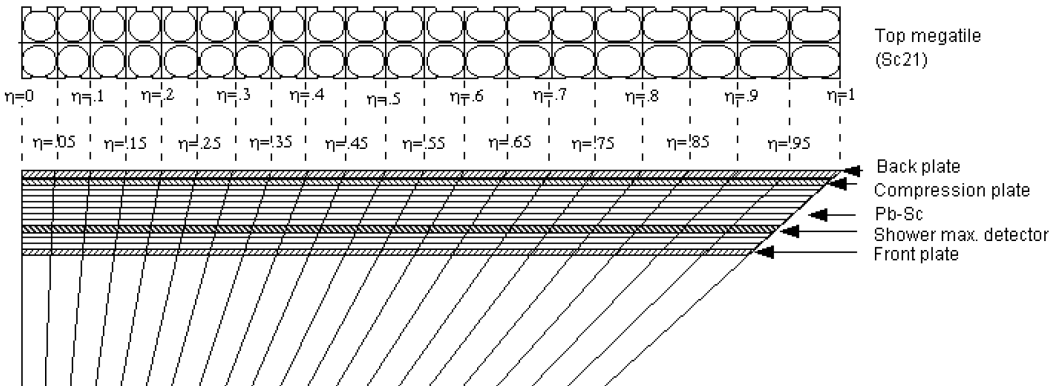

Figure 3.5: Side view of calorimeter module showing the orientation of towers toward interaction region. Taken from Ref. [163]

The BEMC is segmented into 4800 towers and every tower is oriented in the direction of the interaction point. Since measurements, mentioned above, require precise reconstruction with high spatial resolution of electromagnetic shower. The shower maximum detectors (SMD) was implemented within the BEMC. The SMD provides this resolution of shower distributions.

3.2.3 BSMD

While the BEMC towers provide precise energy measurements for isolated electromagnetic showers, the high spatial resolution and shower profile information provided by the SMD (see Figure 4.8) is essential for π^0 reconstruction, direct gamma, and electron identification. The SMD is a wire proportional counter-strip readout detector using gas amplification. The strips are perpendicular to each other.

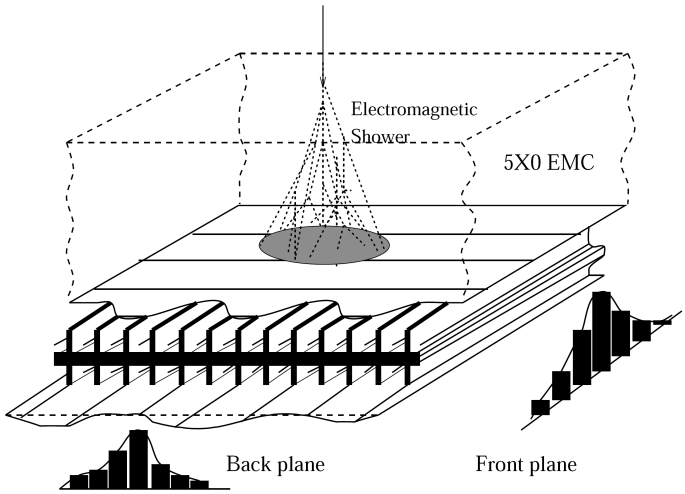

Figure 3.6: Schematic illustration of the double layer BEMC SMD. Two independent wire layers image the shape of electromagnetic showers in the η- and ϕ-directions. Taken from Ref. [163]

Chapter 4

Analysis of Non-photonic Electrons in Cu+Cu Collisions at $\sqrt{s_{NN}}$=200 GeV

The collision system measured in 2005 at RHIC was Cu+Cu at $\sqrt{s_{NN}}$ = 200 GeV. The total amount of collected events by STAR was 51,6M events with minimum bias triggered and 23M so-called High Tower triggered events[1].

Since Cu ions are smaller then previously measured Au ions, the analysis of the Cu+Cu collision system can provide the system size dependence of previously observed effects related to heavy flavor physics such as the suppression of the non-photonic electron production. The non-photonic electrons in Cu+Cu collision at $\sqrt{s_{NN}}$ = 200 GeV has been studied in [174]. In this chapter, we would like to present the study of possible modification of the away-side peak in the electron-hadron correlation function in this system. Similar studies using different method has been recently reported in [175]. In following sections, the details of all steps in the analysis and preliminary results are presented.

4.1 Event Selection

The non-photonic electron analysis was restricted to events with Z axis component (along beam axis) of primary vertex (vertex Z) from -20 cm to 20 cm from the detector mid-point. Figure 4.1 shows this distribution together with selection cuts. The reason for this cut is an observation that, in a larger distance than 20 cm, a huge amount of photon conversion electron is produced due to interactions in support construction [176].

The reference multiplicity[2] cut is another event selection criterion. The reference multiplicity determines the collision centrality. In Cu+Cu collision, the reference

[1] High Tower triggered events contains the subset of events with so-called High Tower (HT) trigger events. In there events at least one segment of the BEMC (tower) has to have deposited energy above defined threshold.

[2] The reference multiplicity is defined as the number of tracks satisfying the following requirements: Flag> 0 (a basic track reconstruction quality requirement); distance to closest approach to the primary vertex $<$ 3 cm; number of fit points in the TPC $\geq$ 10; -0,5 $< \eta <$ 0,5

multiplicity larger than 14 particles defines centrality 0 - 60%. Figure 4.2 shows the reference multiplicity distribution. For final analysis we select 0 - 20 % most central events with reference multiplicity > 98.

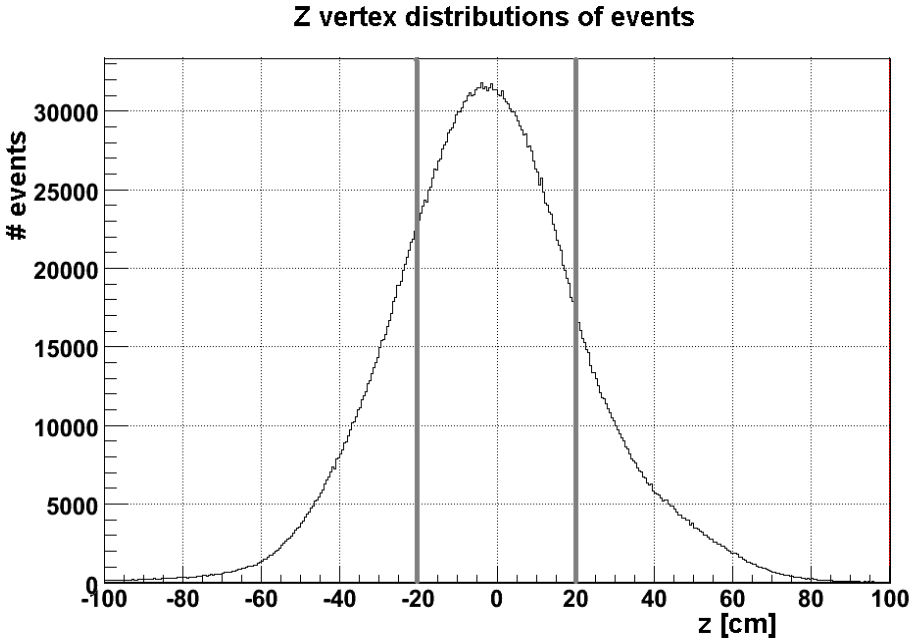

Figure 4.1: The primary Z vertex distribution.

In our analysis, we have used subset of events: High Tower triggered event, that contains events with special High Tower trigger. In High Tower data, over 3,6M events was measured with this trigger and about 2,2 M events passed above mentioned event selection.

4.2 Track Selection

The TPC is the main tracking detector in STAR. The tracks are reconstructed from registered hits in the readout system of the TPC. These points are used to fit the trajectory. In the order to ensure of the good track quality, the Number of fit points (Nfit) cut is used. The distribution of Number of fit points is depicted in Figure 4.3. The tracks reconstructed from more than 20 points are accepted. There is the upper limit of fit points (50 points) due to eliminating double counting of split tracks. For the elimination of double counting of split tracks, the Number of fit points/Number of maximum points cut is also used (Nfit/NmaxPoins $> 0{,}52$).

Additionally in order to avoid the large conversion background from the detector material, only the tracks with $|\eta| < 0{,}7$ are selected, since conversion background comes mainly from other vertices than primary vertex. The global DCA[3] cut (gDCA $< 2{,}0$ cm) is used also for elimination of the photonic electron background.

[3]gDCA is a distance to primary vertex

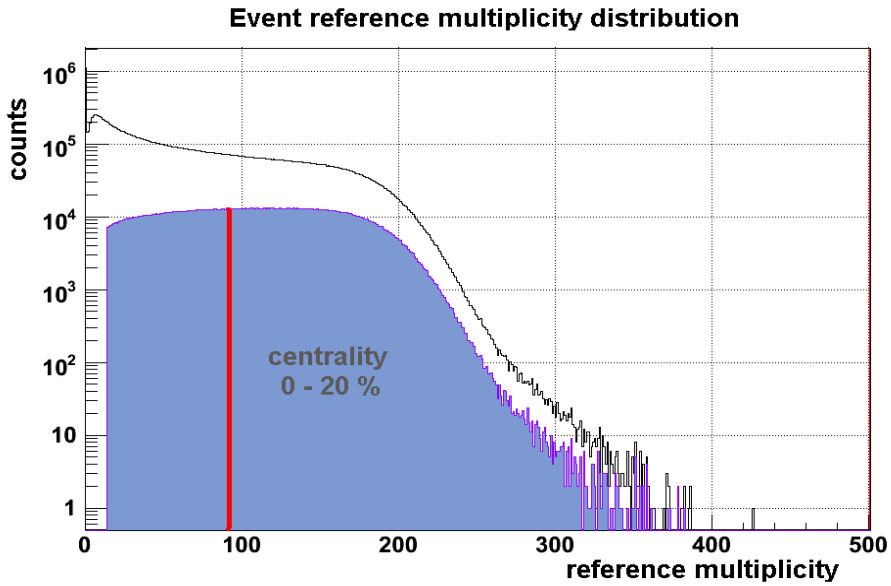

Figure 4.2: The reference multiplicity (refmult) distribution. The shaded area is the refmult $>$ 14 and after application of the vertex Z cut. The area right of line shows the 20% most central events (refmult $>$ 98)

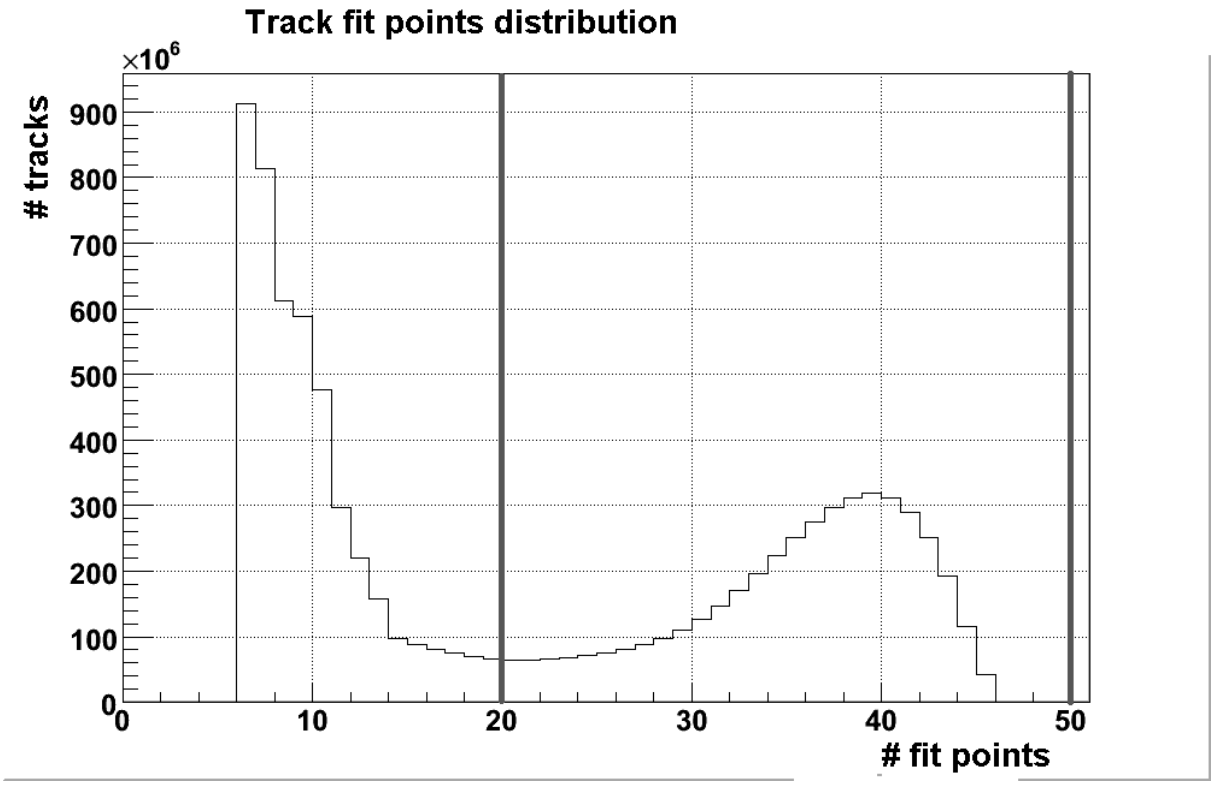

Figure 4.3: The distribution fit points used to reconstruction of tracks with the selection cuts 20 $<$ Number of fit points $<$ 50.

4.3 Electron Selection

The main goal of electron identification is to distinguish electrons and other hadrons, mainly pions. The TPC measurement of the ionization energy loss, dE/dx, for charged tracks is utilized to identify electrons. The distribution of dE/dx against momentum is plot in Figure 4.4. How we can see the electron band crosses the hadron bands. In order to avoid this crossing, for easier distinguishing electrons and hadrons, we select only particles with momentum $p > 1,5$ GeV. The TPC alone cannot deliver definitive information for the electron identification. Therefore the BEMC is also used for the identification of electrons.

In the BEMC, particles deposit specific amount of their kinetic energy. Electrons create wide electromagnetic showers in the BEMC towers and deposit almost theis entire energy therein, while hadrons deposit only its small part and create narrow showers therein.

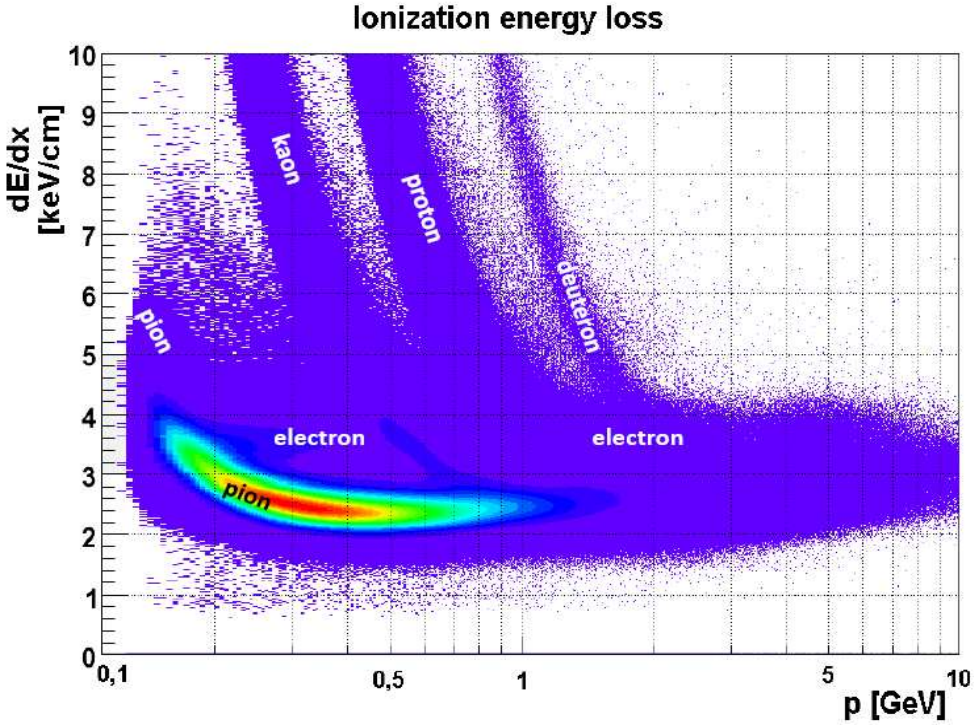

Figure 4.4: Charged particle ionization energy loss in TPC.

The TPC tracks are projected onto the BEMC. However, more than one reconstructed BEMC hit (tower) can be associated with one TPC track. On the other hand, more than one TPC track can share one BEMC tower. We selected those tracks that have at least one associated tower with non-zero deposited energy (i.e. cut BEMC projection > 0).

The ratio p/E, where p is the TPC track momentum and E is the energy deposited in the BEMC, is used as an electron identifier. How it was mentioned above,

electrons deposit almost whole their energy, therefore electron p/E should be approximately equal to one. For hadrons, p/E is much larger then one, due to the small deposited energy in the BEMC. The p/E cut ($0 < p/E < 2$) can keep most of the electrons going into the BEMC and reject a large amount of hadrons. The p/E distribution is depicted in Figure 4.5.

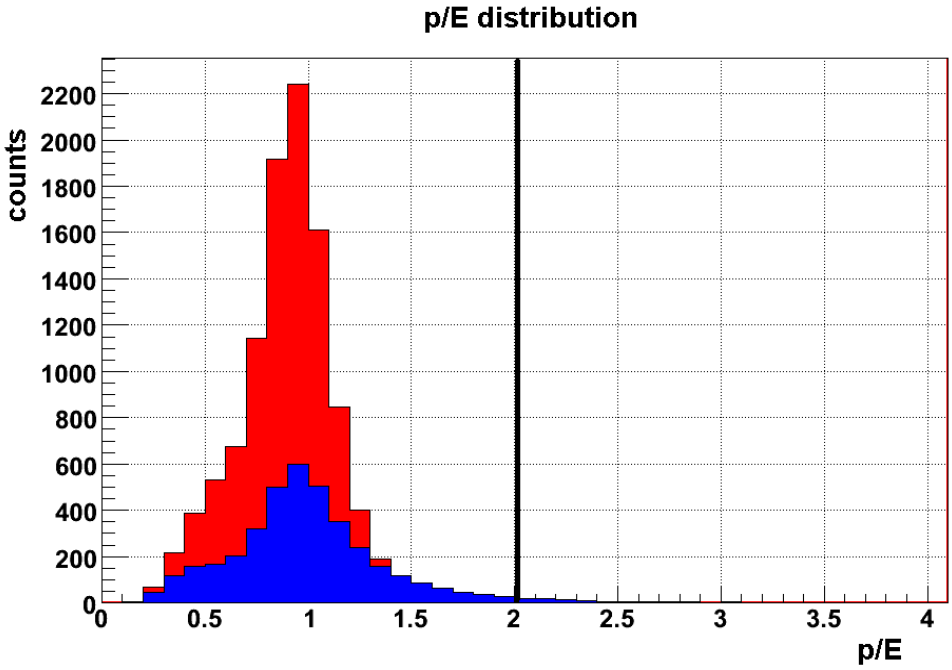

Figure 4.5: The p/E distrubution. The electron p/E distribution is red shaded and the hadron impurity of the electron sample is blue shaded. The vertical line shows the upper limit of the p/E cut.

From the signals in SMD, clusters are reconstructed. Size of the cluster is related to the size of the electromagnetic shower. Electrons and pions are distinguished also in accordance with the cluster size of their electromagnetic showers created in the BEMC. The distribution of cluster size in ϕ and η direction for electrons and hadrons are plot in Figure 4.6 and Figure 4.7.

For distinguishing electrons and hadrons, the SMD cluster size cut is utilized (SMD cls ≥ 2) in ϕ and η.

The distribution dE/dx against momentum after all selectrion cuts is depicted in Figure 4.8.

Figure 4.9 shows, how the dE/dx distribution changes when the BEMC and SMD cuts are used cut-by-cut. We can see that these cuts strongly reduced the hadron contamination, however, number of electrons stayed almost unchanged. The $dE\,dx$ distribution can be fit with Gaussians representing hadrons and electrons in final sample. The fit is depicted in Figure 4.10. The hadron impurity of electron sample can be determined (shaded area in Figure 4.10 - $\sim 3,3\%$). Now, electrons can be distinguished from hadrons by dE/dx cut: 3,31 keV/cm $< dE/dx <$ 4,64 keV/cm.

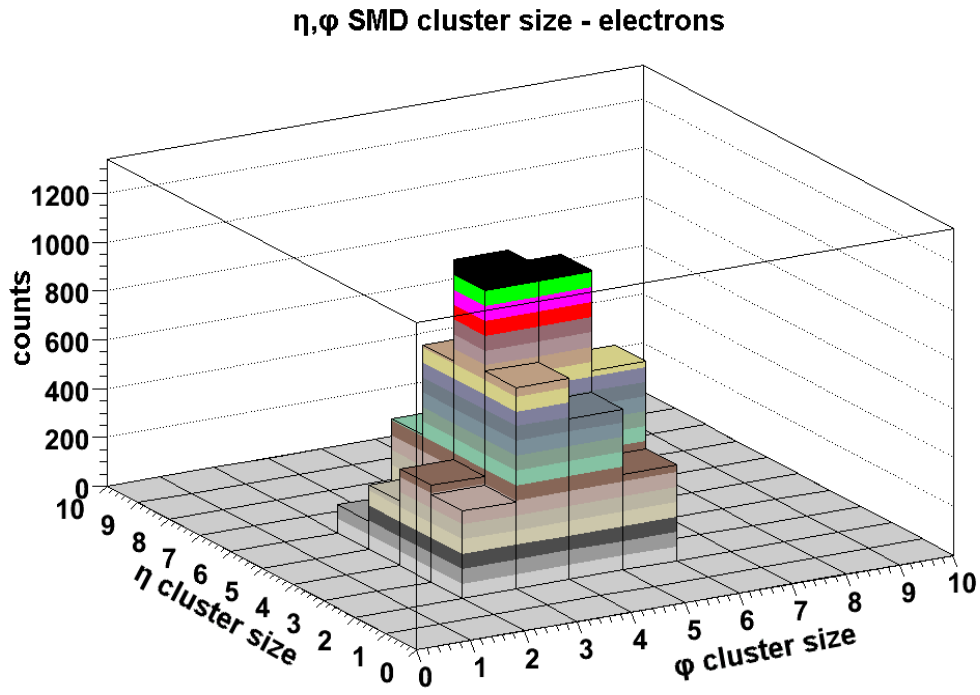

Figure 4.6: The SMD cluster size in ϕ and η direction for electrons.

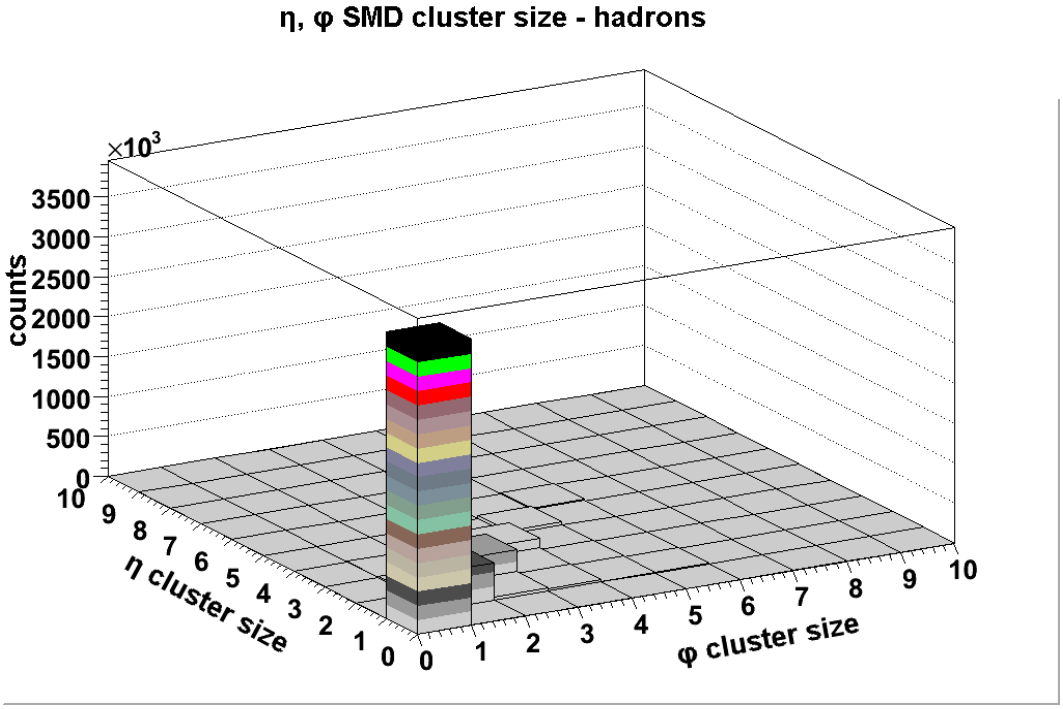

Figure 4.7: The SMD cluster size in ϕ and η direction for hadrons.

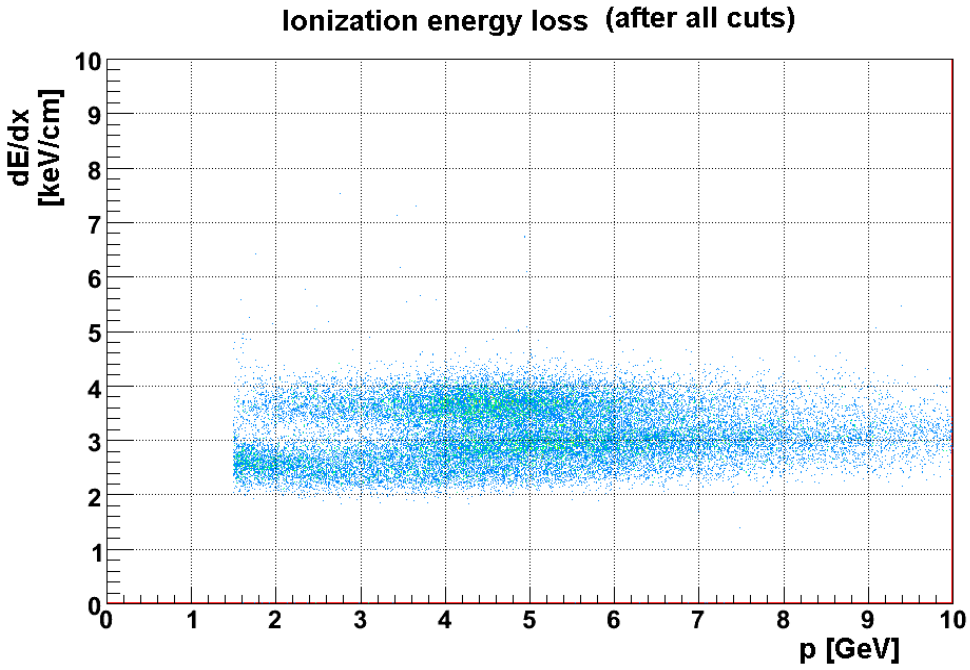

Figure 4.8: Charged particle ionization energy loss in TPC after all selection cuts.

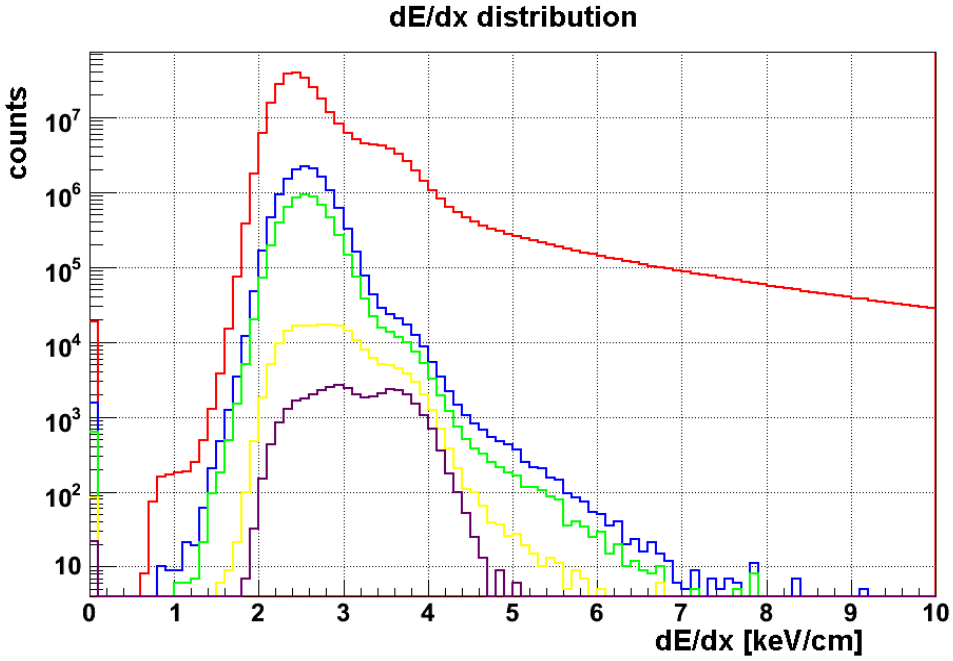

Figure 4.9: The evolution of the dE/dx distribution after applying selection cuts. The red curve shows dE/dx of all TPC tracks. The blue curve is dE/dx after $p > 1,5$ GeV cut, the green after the BEMC projection cut. Yellow curve after p/E cut, and violet curve is dE/dx after SMD cluste size cut.

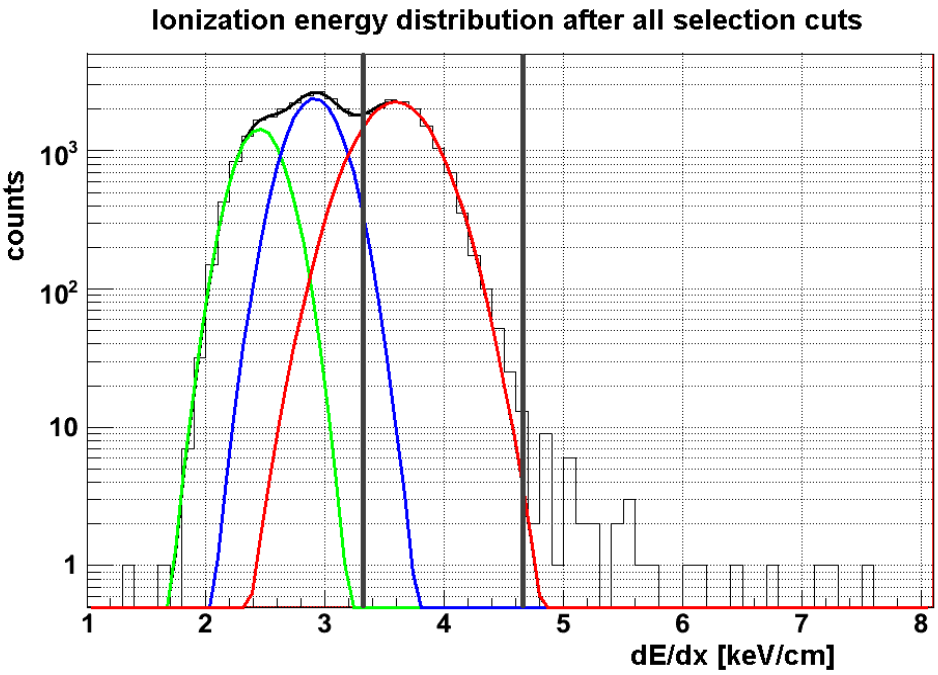

Figure 4.10: The dE/dx distribution fit by Gaussians to distinguish hadrons (green), pions (blue), and electrons (red) contribution in track sample.

After applying all selection criteria we found 3968 inclusive electrons in the 0 - 20% most central collisions. This is 0,018 electrons/per event. The p_T spectrum of reconstructed inclusive electrons[4] is plot in Figure 4.11. The spectra are not normalized and also not corrected for electron identification efficiency. This was not necessary for further analysis of azimuthal correlations.

4.4 Photonic Electron Background Rejection

The inclusive electron sample consist of both the non-photonic electrons and a large amount of the background electrons not arising from the heavy mesons decays. There are several sources of the background electrons:

- photon conversion ($\gamma \rightarrow e^+e^-$) in detector and support structure material, the conversion photons come dominatly from π^0 and η decays ($\pi^0, \eta \rightarrow \gamma\gamma$).
- scalar mesons (π^0 and η) Dalitz decays: $\pi^0, \eta \rightarrow \gamma e^+e^-$
- vector mesons (ρ, ω, ϕ) Dalitz and/or dielectron decays: $\rho, \omega, \phi \rightarrow e^+e^-$
- weak kaon decay K_{e_3}: $K \rightarrow \pi^0 e\nu$
- Drell-Yan: $\gamma^* \rightarrow e^+e^-$

[4] in this analysis by electrons we mean both electrons and positrons.

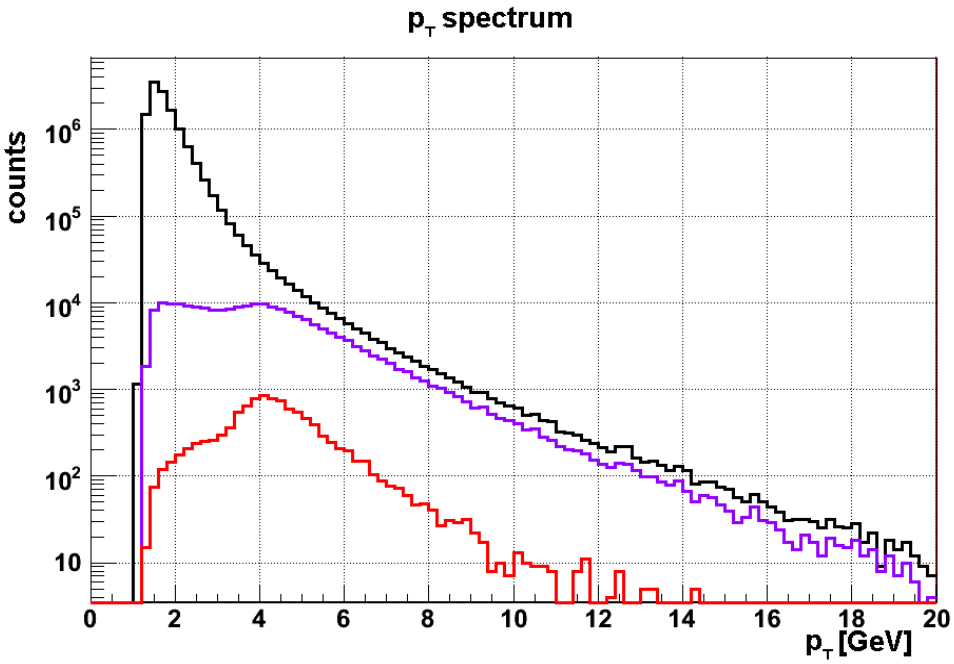

Figure 4.11: Transverse momentum spectrum of all TPC tracks (black), track that could trigger High Tower event (violet), all identified inclusive electrons (red).

- other: direct photon conversion, heavy quarkonium decays, thermal electrons

The dominant sources of photonic electron background are photon conversion, π^0 and η Dalitz decays [177], others are negligible [178, 179].

Since background photonic electrons are always produced in e^+e^- pairs, we try to reconstruct the yield of this pairs. Therefore we are looking for the electron partner with the opposite charge sign (unlike-sign electrons) and then the invariant mass of such pair is calculated as

$$M_{inv} = 2\sqrt{p_1 p_2} sin\frac{\alpha}{2}, \tag{4.1}$$

where p_1, p_2 are particle momentum magnitudes, and α is the angle between two tracks.

Firstly, we tag one electron (to use the electron identification criteria) and we are looking for the partner track satisfying the following conditions:

- opposite charge
- $p > 0,1$ GeV
- dE/dx: 2,97 - 4,64 keV/cm
- dca[5] < 2 cm

[5]dca here mean distance of closest approach of two tracks

This conditions for particle track are chosen to suppress the same combinations with hadron, but keep the most of true electron partners.

The invariant mass is computed for all possible partners satisfying these criteria. The invariant mass distribution of electron-positron pairs is plot in Figure 4.12. This distribution contains both the true photon conversion pairs (further photonic electrons) and also the fake combinations. This combinatorial background rises from combinations of electrons with hadrons, but also uncorrelated electron-positron pairs (i.e. from two independent photon conversions) and/or also from the non-photonic electrons which can be falsely identified as photonic electrons.

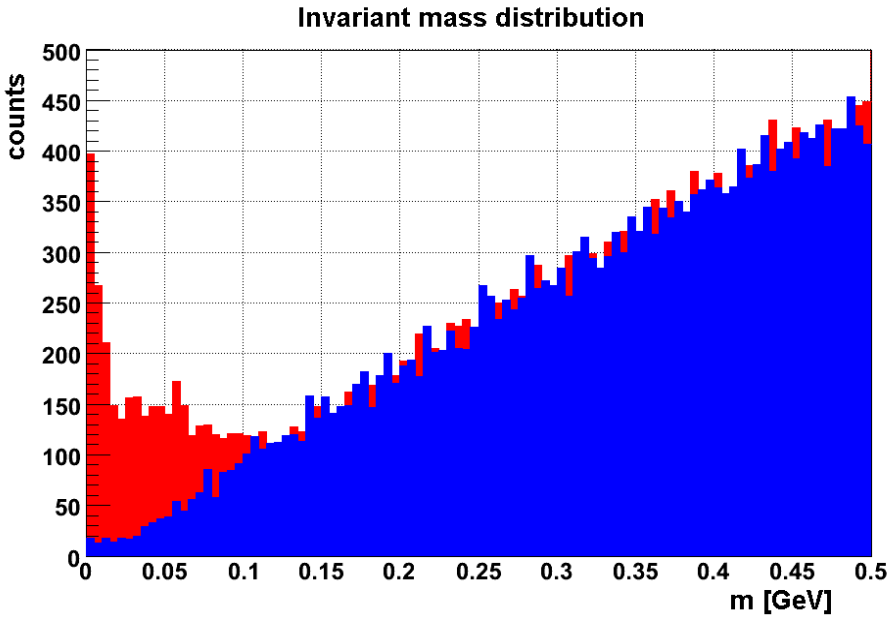

Figure 4.12: The electron-positron invariant distribution. The invariant mass of the unlike-sign electrons is red shaded and the combinatorial background (i.e. like-sign pairs) is blue shaded.

The combinatorial background can be determined by the calculation of the invariant mass of the same-sign (like-sign) electron pairs (i.e. e^+e^+ and e^-e^-).

The invariant mass of the photonic electrons is given by the subtraction of the like-sign electrons from the unlike-sign electrons. The photonic invariant mass is depicted in Figure 4.13. The high peak about zero comes from the photon conversion. The broad tail comes from the π^0 Dalitz decays and it is ending about the rest mass of π^0. As the photonic electrons, we accepted the electrons in pairs with the invariant mass less than 150 MeV. In Figure 4.13, this is highlight by the vertical line.

Because the reconstruction of all conversion pairs is impossible (e.g. one member of the electron-positron pair is not reconstructed in the detector, i.e. it is forward directed or it can be absorbed in detector material), the real number of the photonic electrons N_{PHOT} is given by

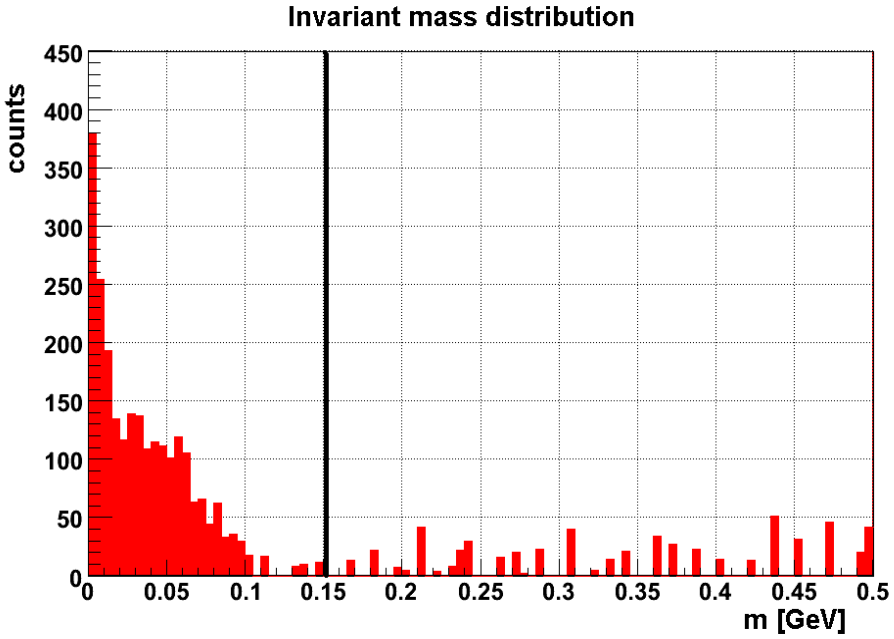

Figure 4.13: The photonic electron invariant mass distribution. The peak about zero comes from photon conversion and the broad tail comes from Dalitz decays of π^0. By vertical line, the invariant mass cut is highlight.

$$N_{PHOT} = \frac{N_{RECO}}{\varepsilon} = \frac{N_{UNLIKE} - N_{LIKE}}{\varepsilon}, \tag{4.2}$$

where N_{RECO} is the number of reconstructed photonic electrons, N_{UNLIKE} is the number of the unlike-sign electrons, N_{LIKE} is number of the like-sign electrons, and ε is the reconstruction efficiency which can be determined by the numerical simulations [knospe]. We use $\varepsilon = 0{,}65$.

4.5 Non-photonic Electron - hadron Correlarions

The main goal of this work is the study of properties of the hot nuclear matter by two-particle azimuthal correlations of the non-photonic electrons (3 GeV $< p_T <$ 6 GeV) with charged hadrons (e-h correlations) with low momenta: 0,15 GeV $< p_T <$ 1,00 GeV in the most central Cu+Cu collisions (centrality 0 - 20%). The background to the non-photonic e-h correlations is given by photonic e-h correlations.

The non-photonic e-h correlations are given by

$$\left(\frac{dN}{d\Delta\phi}\right)_{NON} = \left(\frac{dN}{d\Delta\phi}\right)_{INC} - \left(\frac{dN}{d\Delta\phi}\right)_{PHOT}, \tag{4.3}$$

where $\left(\frac{dN}{d\Delta\phi}\right)_{INC}$ is the inclusive e-h correlations, and $\left(\frac{dN}{d\Delta\phi}\right)_{PHOT}$ is the photonic e-h correlations.

The inclusive electrons include all tracks passed the electron identification cuts. The inclusive e-h correlations are depicted in Figure 4.14.

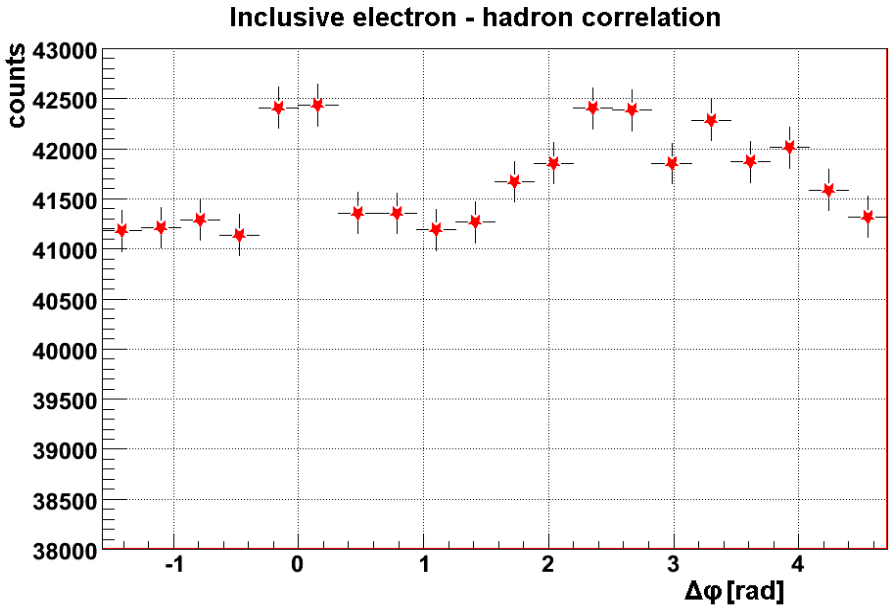

Figure 4.14: Inclusive electron-hadron correlation ($3,0\text{GeV} < p_T^{electr} < 6,0\text{GeV}$ and $0,15\text{GeV} < p_T^{hadr} < 1,00\text{GeV}$),the most central (centrality 0 - 20%) Cu+Cu collisions at $\sqrt{s_{NN}}$=200 GeV

The photonic e-h correlations are given by

$$\left(\frac{dN}{d\Delta\phi}\right)_{PHOT} = \frac{\left(\frac{dN}{d\Delta\phi}\right)_{UNLIKE} - \left(\frac{dN}{d\Delta\phi}\right)_{LIKE}}{\varepsilon}, \tag{4.4}$$

where $\left(\frac{dN}{d\Delta\phi}\right)_{UNLIKE}$ is the unlike-sign e-h correlations (see Figure 4.15), $\left(\frac{dN}{d\Delta\phi}\right)_{LIKE}$ is the like-sign e-h correlations (see Figure 4.16), and ε is the photonic electron reconstruction efficiency. For clarification: unlike-sign (like-sign) e-h correlations are the correlations of electrons with the oposite (same) charged tracks that build the pair with invariant mass < 150 MeV.

The non-photonic e-h correlations are depicted in Figure 4.17.

4.6 Correction to Azimuthal Correlation Function

There are several important correction to measured e-h azimuthal correlation function that has to be made. The read-out section of TPC is segmented into twelve segments. The connections between two segments make ”dead regions” of TPC (see Figure 4.18).

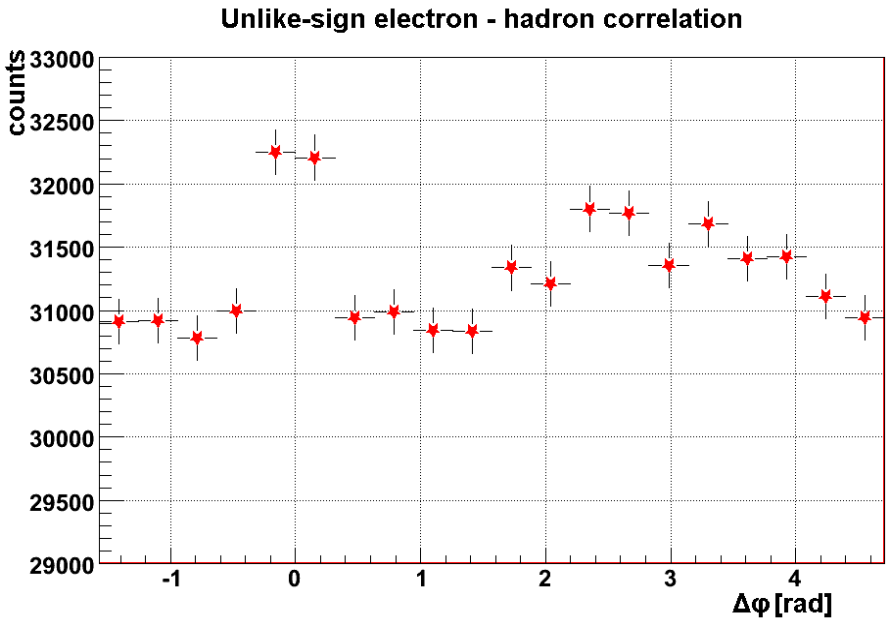

Figure 4.15: Unlike-sign electron hadron correlation ($3,0\text{GeV} < p_T^{electr} < 6,0\text{GeV}$ and $0,15\text{GeV} < p_T^{hadr} < 1,00\text{GeV}$), the most central (centrality 0 - 20%) Cu+Cu collisions at $\sqrt{s_{NN}}$=200 GeV

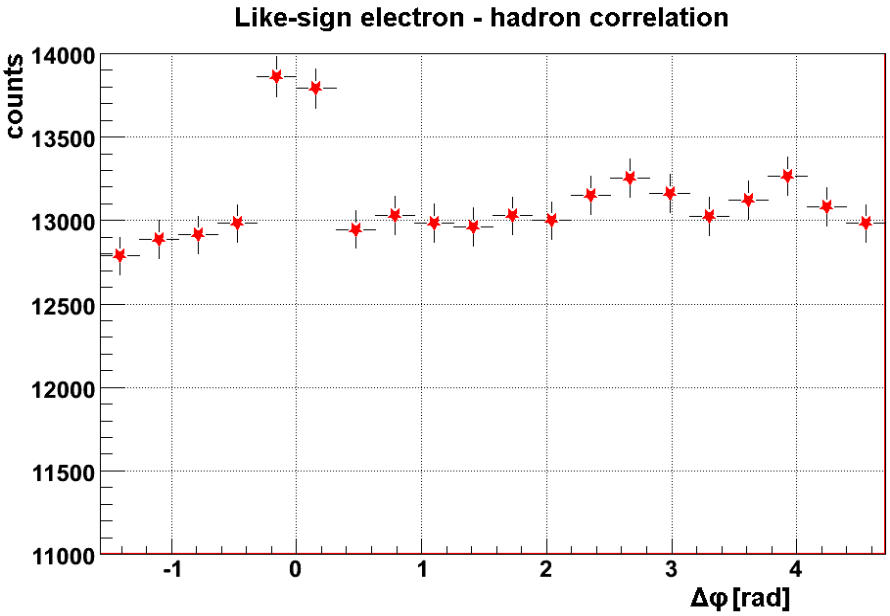

Figure 4.16: Like-sign electron hadron correlation ($3,0\text{GeV} < p_T^{electr} < 6,0\text{GeV}$ and $0,15\text{GeV} < p_T^{hadr} < 1,00\text{GeV}$), the most central (centrality 0 - 20%) Cu+Cu collisions at $\sqrt{s_{NN}}$=200 GeV

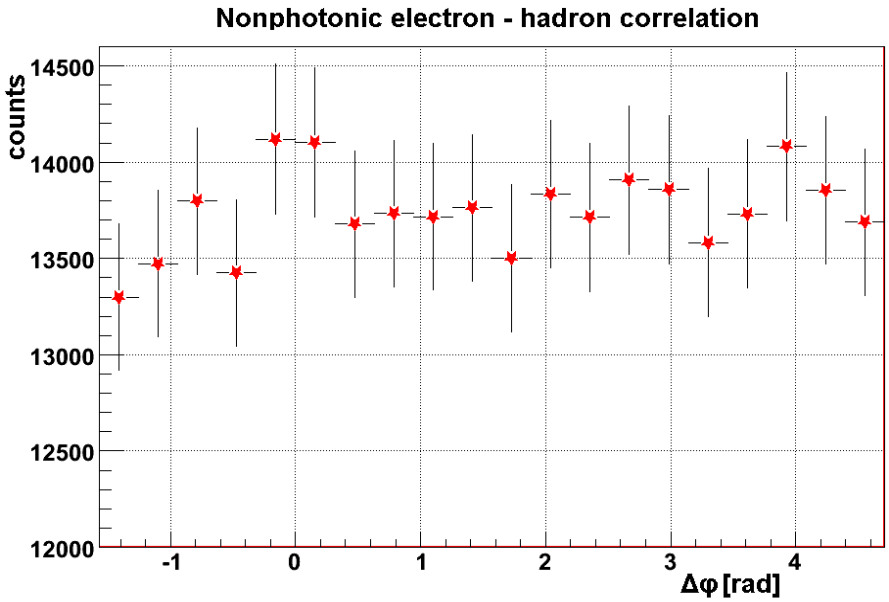

Figure 4.17: Non-photonic electron hadron correlation (3, 0GeV< p_T^{electr} < 6, 0GeV and 0, 15GeV< p_T^{hadr} < 1, 00GeV), the most central (centrality 0 - 20%) Cu+Cu collisions at $\sqrt{s_{NN}}$=200 GeV, no corrections

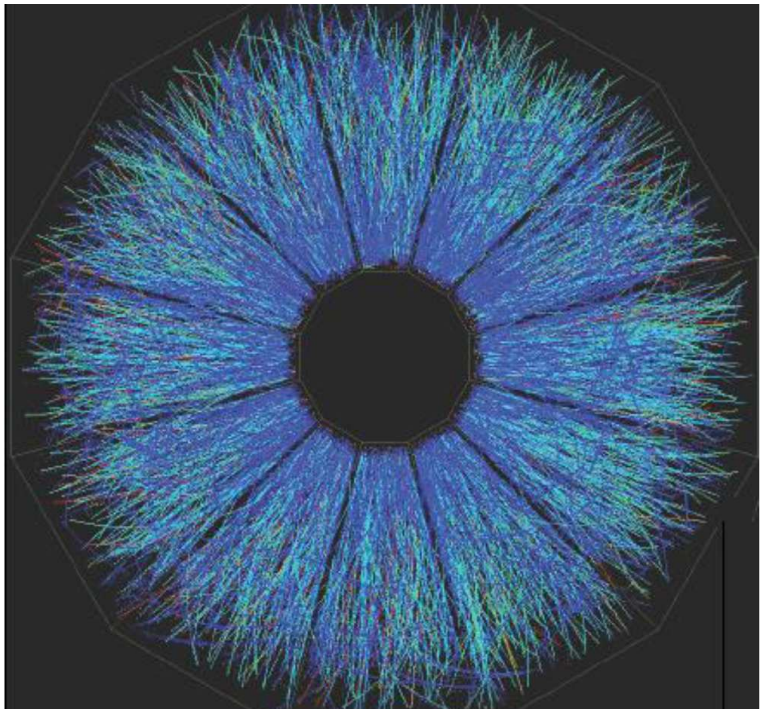

Figure 4.18: The central collision tracks in the STAR TPC viewed in the plane perpendicular to the beam axis. There are clearly seen dead regions between two read-out segments and also in the particle azimuthal distributions.

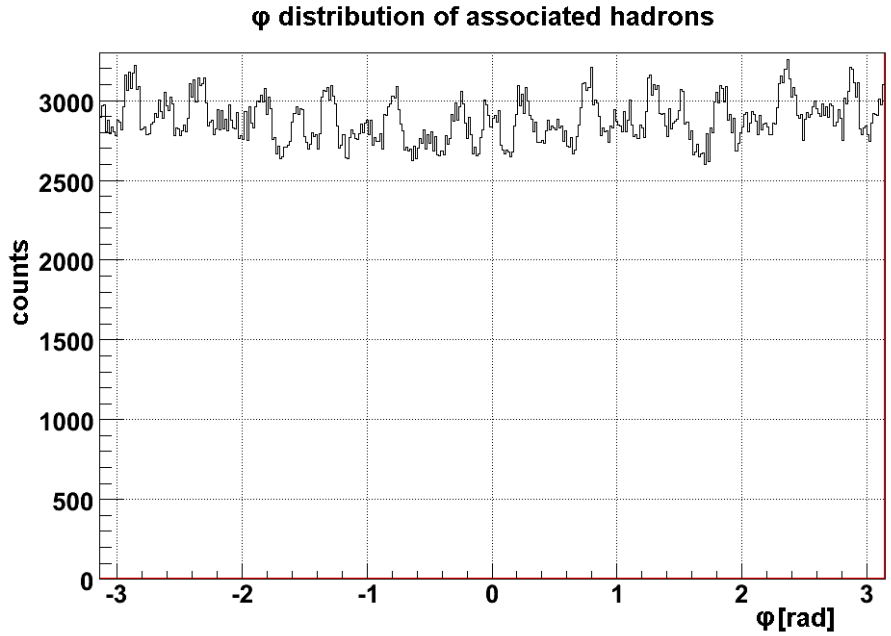

Figure 4.19: Azimuthal distribution of associated hadrons with 0,15 GeV $< p_T <$ 1,00 GeV.

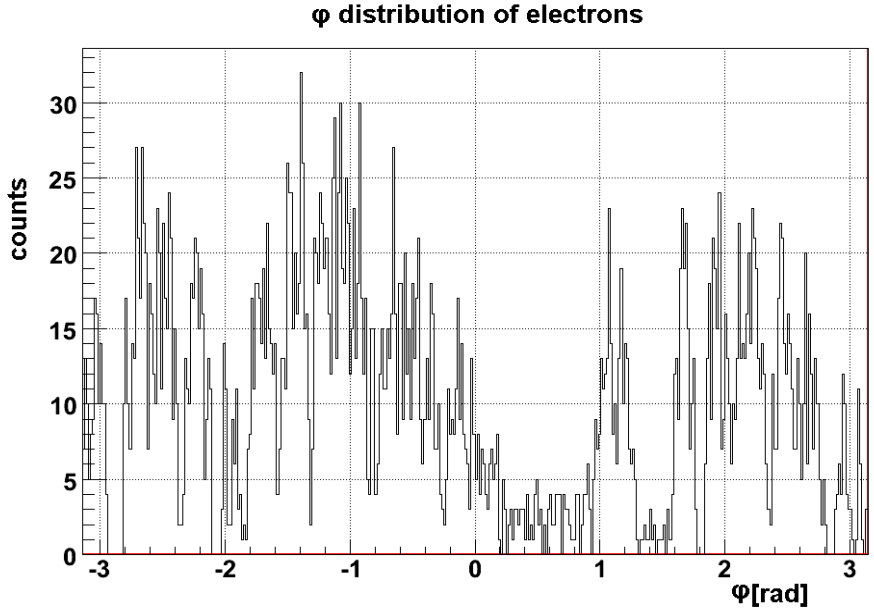

Figure 4.20: Azimuthal distribution of trigger electrons with 3,0 GeV $< p_T <$ 6,0 GeV. The reason that distribution is not flat comes from holes in BEMC acceptance.

The tracks overlaped with this connection cannot be reconstructed and this is also reflected in azimuthal angle (ϕ) distribution of hadrons (Figure 4.19) and electrons (Figure 4.20). The ϕ-distribution of electrons also reflect the BEMC acceptance (i.e. non-working parts of the BEMC). Therefore the e-h correlations are affected by these effect and they must be corrected on them. This can be done by the mixing event method (further mixing events). We suppose, that the ϕ-distributions are the probability distribution functions (PDF). For mixing, we have randomly selected one electron with ϕ_1 from the electron PDF and one hadron with ϕ_2 from the hadron PDF. The azimuthal mixing event ($\phi_1 - \phi_2$) distribution is plot in Figure 4.21. The number of randomly selected ϕ_1, ϕ_2 (electron-hadron) pairs should be minimally about one order larger than the number of measured electron-hadron pairs. For correction purpose the mixing event ($\phi_1 - \phi_2$)-distribution is normalized to one.

The mixing event corrections of e-h correlations are applied bin-by-bin by dividing e-h correlations by the normalized ($\phi_1 - \phi_2$)-distribution. Figure 4.22 shows the e-h correlations after the mixing event corrections.

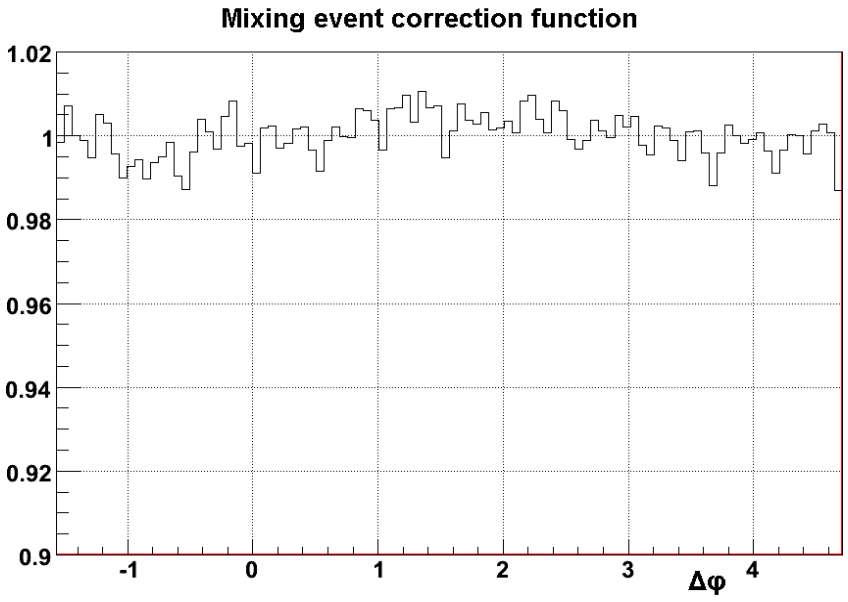

Figure 4.21: The mixed event correction function.

Because we are interested only in the angle modification of the away-side peak, that should be symmetrical distributed around the π-axis, we can mirror (and so symmetrize) the e-h correlations around zero- and π-axis. By the symmetrizing of correlations, we enlarge the statistics. After this, the double hump structure of the away-side peak is clearly seen (see Figure 4.23).

The last step is the elliptic flow v_2 subtraction. The flow contributing to azimuthal correlation is given by

$$\frac{dN}{d\Delta\phi} = A\left(1 + 2v_2^e v_2^h cos\left(2\Delta\phi\right)\right), \tag{4.5}$$

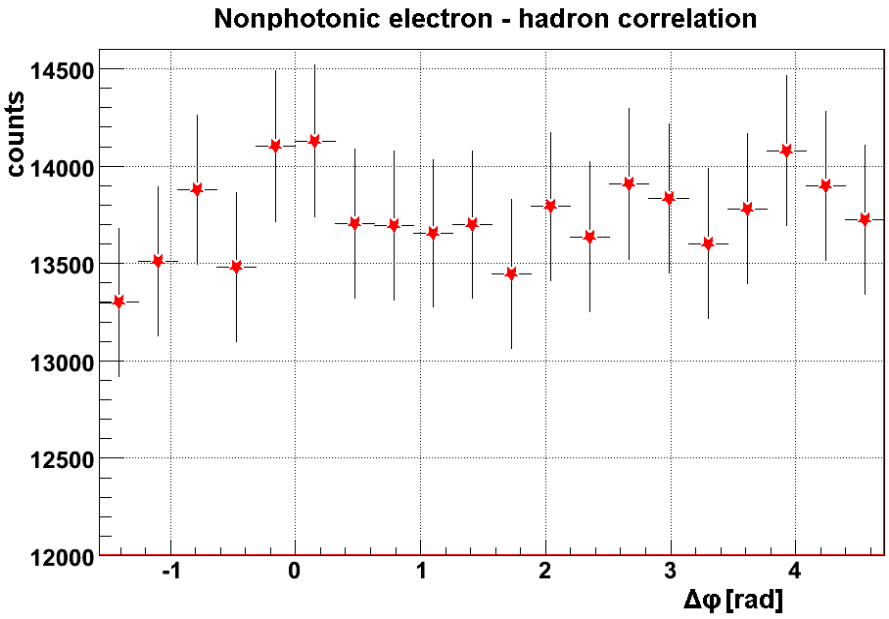

Figure 4.22: The non-photonic correlations after application the mixing event correction.

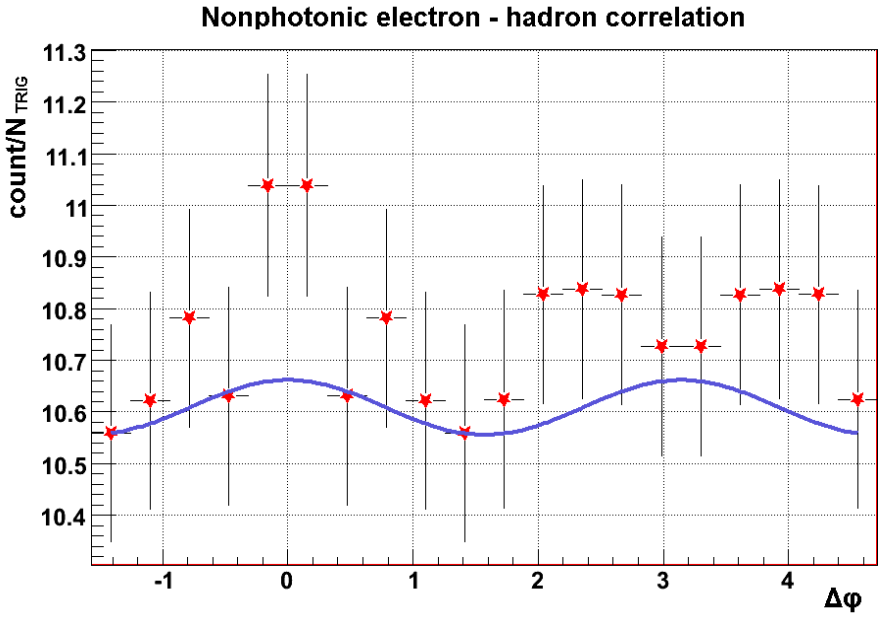

Figure 4.23: The non-photonic correlations after mixed event corrections. The correlation function is mirrored around the zero and π axis. There is also figured the elliptic flow.

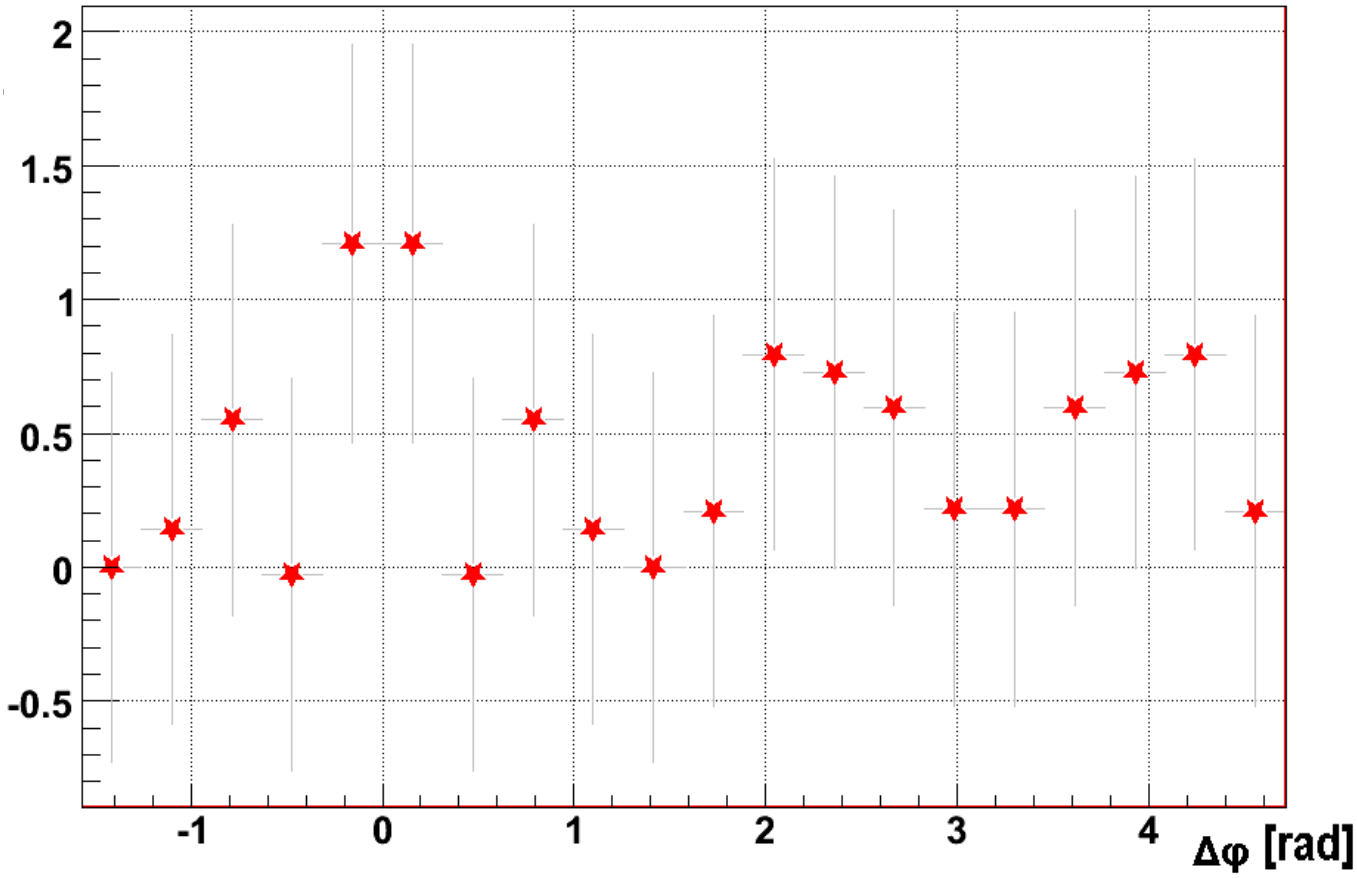

Figure 4.24: The non-photonic electron - hadron azimuthal correlation function ($3,0\text{GeV} < p_T^{electr} < 6,0\text{GeV}$ and $0,15\text{GeV} < p_T^{hadr} < 1,00\text{GeV}$) with the subtracted elliptic flow for the most central (centrality 0 - 20%) Cu+Cu collisions at $\sqrt{s_{NN}}$=200 GeV

where v_2^e is the electron flow and v_2^h id flow of charges hadrons. We assume that $v_2^e = v_2^h = v_2 = 0,05$ for 20% most central collisions. The parameter A is determined by the ZYAM[6] method [180, 181] (flow is going through the minimum of the correlation function). The final azimuthal e-h correlations are depicted in Figure 4.24. Final spectra are normalized to number of trigger event (number of electrons with 3,0 GeV$< p_T <$ 6,0 GeV) and also bin size (bin size = 0,314115).

All error bars plotted in histograms are maximal statistical errors. The errors are ,in reality, smaller, because inclusive and photonic statistical errors are correlated. The systematic errors will be further studied.

[6] Zero Yield At Minimum

Chapter 5

Summary and Conclusion

The main aim of this work was the study of interactions of heavy quarks with the medium produced in Cu+Cu collision at $\sqrt{s_{NN}}$=200 GeV. Heavy quarks originate in the early stages of heavy ion collisions, before the formation and thermalization of the hot and dense nuclear medium, and they decay after the hadronization of this medium. Therefore heavy quarks are the excellent probe of the medium properties and therefore it is important to know their in-medium interactions. We have focused on that, how this interaction affects the form of the azimuthal correlation function. Heavy quarks can be indirectly indentified via electrons coming from their weak (semi-leptonic)decays. That is why the electron-hadron correlations were performed in this work.

The nonphotonic electron-hadron correlations are plot in Figure 4.24. We can see, the near-side peak around $\Delta\phi = 0$ in the azimuthal correlation function. This means that electrons coming from heavy quark decays are correlated with low-p_T hadrons from the near-side jet. The away-side peak modification is observed in the azimuthal correlation function. The similar double hump structure was observed in the azimuthal correlations of hadrons. This can indicate similar response of nuclear matter to passage of heavy quarks as of light quarks. Preliminary studies presented here will be continuing. We plan to extract the corrected nonphotonic electron yield, study the systematics errors and extend this study to Au+Au collisions.

How it was discussed in the section 1.1.2, this double hump structure can be explained by the creation of the super sonic shock wave and Mach cone by quark passage through a dense medium. For example, for the QGP and its speed of sound equal to 33% of the speed of light, it has been proposed that humps are located at $\Delta\phi = \pi \pm 1,2$ rad. This is actually observed in the electron-hadron correlation function. Our results are in very good agreement with results reported recently in ref. [175].

Appendix A

Azimuthal Correlations

In the proton-proton collision, the hadron jet can be directly observed and reconstructed (see Figure A.1). However, in the central heavy ion collision due to a high particle multiplicity, this is, in practice, up to now not possible (see. Figure A.2). Therefore the properties of jets have to be studied otherwise. The two-particle azimuthal correlations allow the statistical jet observation. In this method, there is assumed that particles with high p_T (usually $p_T > 3$ GeV) surely belong to jet.

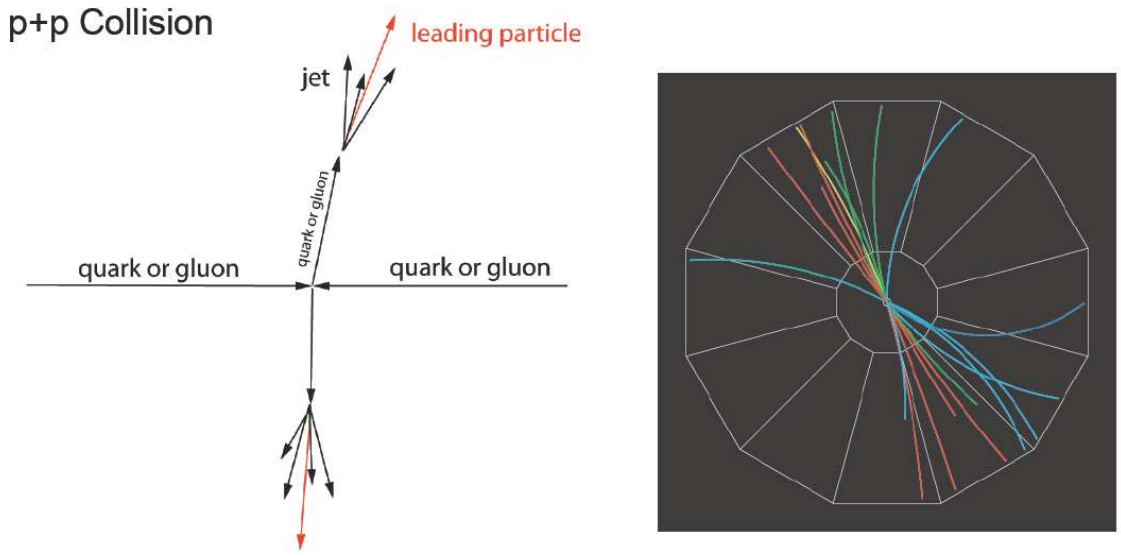

Figure A.1: **Left:**The schematic view of the central p+p collision. **Right:** The p+p collision recorded by the STAR TPC

In the first step, the so-called leading (or trigger) particle (i.e. particle with the highest p_T in event - p_T^{TRIG}) is chosen and the angle ($\Delta\phi$) between this leading particle ant the other particles in event (so-called associated particles with $p_T^{ASSOC} < p_T^{TRIG}$) is determined (see Figure A). If even other particles (associated ones in the first step) have got their $p_T > 3$ GeV, there are considered to be trigger particles

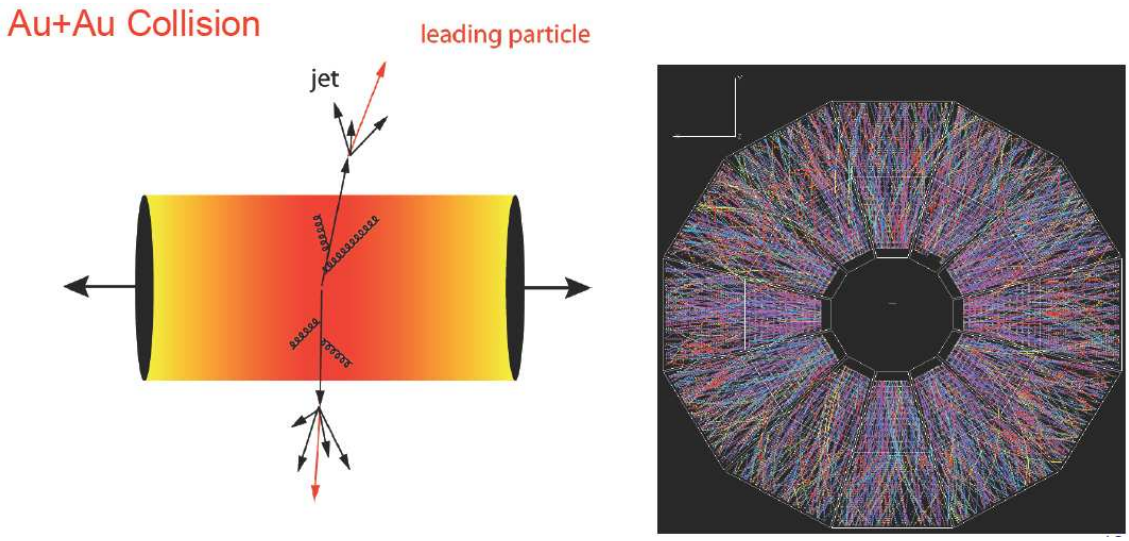

Figure A.2: **Left:**The schematic view of the central Au+Au collision. **Right:** The cental Au+Au collision recorded by the STAR TPC

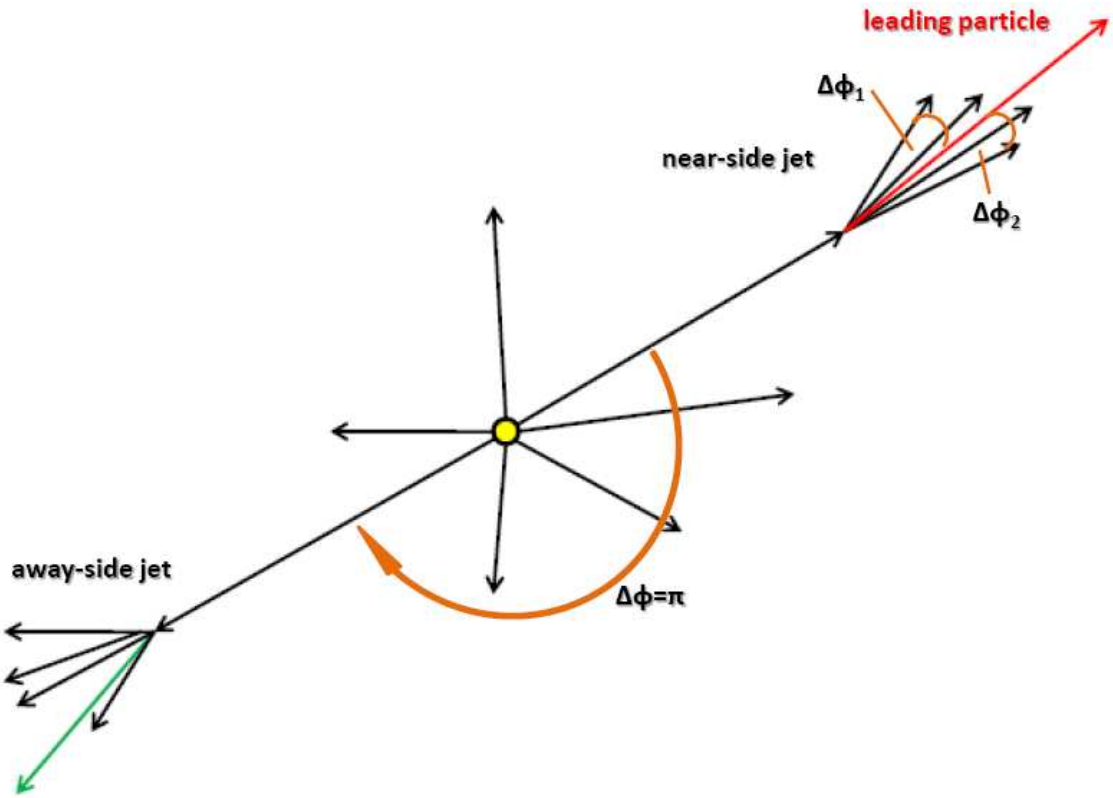

and the same procedure is applied. Finally, the azimuthal correlation function is obtained (see Figure A.3). In this function, two peaks are seen. One peak, around $\Delta\phi = 0$, comes from the near-side jet, i.e. particles contributed to this peak and jet trigger particle come from the same jet. The second peak, (away-side peak), around $\Delta\phi = \pi$, means that associated particles come from the opposite jet then the trigger particle.

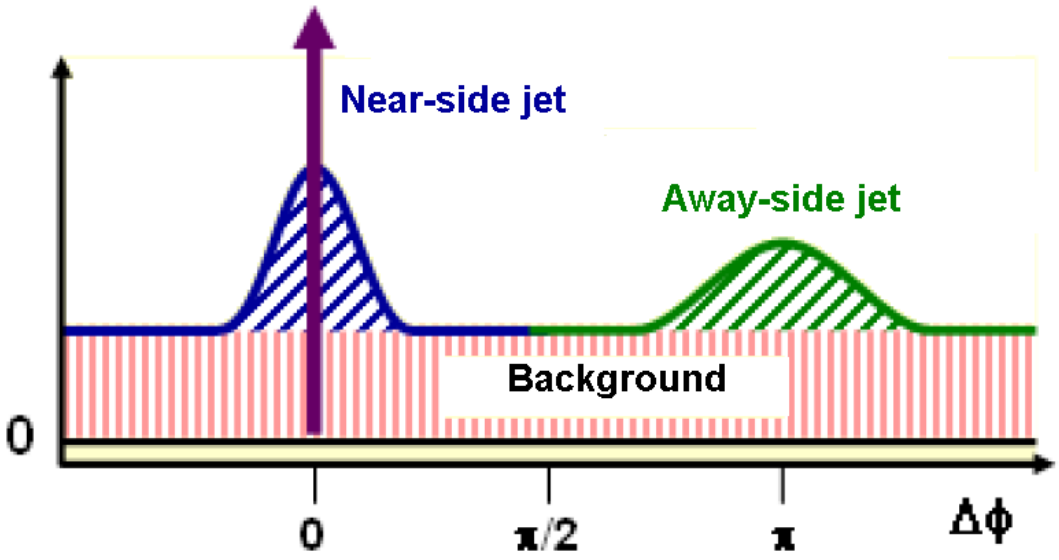

Figure A.3: The azimuthal correlation function usually contains two peaks. Particles belong to one jet with the leading particle (depicted by vertical arrow) form the near-side peak and particles belong to another jet then the leading particle form the away-side peak. The background is formed by a correlation the leading particle with particles belonging to no jet.

Bibliography

[1] F. Wilczek, Ann. Rev. Nucl and Part Sci 32, (1982) 177

[2] H. D. Politzer, Phys. Rev. Lett. 3 (1973) 1346

[3] D. J. Gross and F. Wilczek, Phys. Rev. Lett. 30 (1973) 1343

[4] http://www.gsi.de/fair/experiments/CBM/Phasendiagram.jpg

[5] L.D. McLerran and B. Svetitsky, Phys. Lett. B98, 195 (1981) and Phys. Rev. D24 (1981) 450

[6] J. Kuti, J. Polonyi and K. Szlachanyi, Phys. Lett. B98 (1981) 199

[7] F. Karsch, Lect. Notes Phys. 583 (2002) 209 [hep-lat/0106019]; F. Karsch, E. Laermann, hep-lat/0305025; E. Laermann, O. Philipsen, hep-ph/0303042.

[8] K. Yagi, T. Hatsuda, and Y. Miake, Quark-Gluon Plasma, University Press, Cambridge (2005)

[9] Proceedings of the various 'Quark Matter' conferences, which began in 1981.

[10] H. Satz, Nucl. Phys. A 715 (2003) 3 [hep-ph/0209181] and ref. therein.

[11] H. H. Gutbrod, A. M. Poskanzer, and H. G. Ritter, Plastic Ball Experiments Rep. Prog. Phys. 52 (1989) 1267

[12] C.A. Ogilvie, Nucl. Phys. A 698 (2002) 3c [nucl-ex/0104010]; M.A. Lisa, Nucl. Phys. A 698 (2002) 185c [nucl-ex/0104012]

[13] U. Heinz, M. Jacob, nucl-th/0002042 and ref. therein

[14] K. Blasche, B. Franzke, Proceedings of the 4th European Particle Accelerator Conference, London (1994), edited by V. Suller and Ch. Petit-Jean-Genaz (World Scientific, Singapore, 1994) 133

[15] M. Harrison, T. Ludlam, and S. Ozaki, Nucl. Instr. Meth. Phys. Res. A 499:2-3 (2003) 235 ; M. Harrison, S. Peggs, and T. Roser, Ann. Rev. Nucl. Part. Phys. 52, (2002) 425 ; E. D. Courant, Ann. Rev. Nucl. Part. Phys. 53 (2003) 1

[16] L. McLerran, hep-ph/0202025; J.Nagle, T. Ullrich, nucl-ex/0203007; P. Jacobs, hep-ex/0211031; D. Kharzeev, Nucl. Phys. A 715 (2003) 441c [nucl-th/0211083]; http://www.bnl.gov/rhic/

[17] K. Kajantie, Nucl. Phys. A 715 (2003) 432c ; P. Giubellino, Nucl. Phys. A 715 (2003) 441c ; R.J. Fries, B. Müller, nucl-th/0307043

[18] http://www.gsi.de/zukunftsprojekt/index e.html

[19] J.D. Bjorken, Phys. Rev. D 27 (1983) 140

[20] K. Kajantie, L. McLerran, Ann. Rev. Nucl. Part. Sci. 37 (1987) 293 ; J.W. Harris, B. Müller, Ann. Rev. Nucl. Part. Sci. 46 (1996) 71 [hep-ph/9602235]; S.A. Bass, M. Gyulassy, H. Stöcker, and W. Greiner, J. Phys. G25 (1999) R1 [hepph/9810281]

[21] T. Peitzmann and M.H. Thoma, Phys. Rep. 364 (2002) 175 [hep-ph/0111114]

[22] P.V. Ruuskanen, "Photons and lepton pairs: The deep probes of quark-gluon plasma", in: Particle Production in Highly Excited Matter, H.H. Gutbrod and J. Rafelski (Eds.), NATO ASI Series B: Physics Vol. 303 (1993) 593 (Plenum, New York)

[23] R. Rapp, J. Wambach, Adv. Nucl. Phys. 25 (2000) 1 [hep-ph/9909229]; J.P. Wessels et al. (CERES), Nucl. Phys. A 715 (2003) 262c [nucl-ex/0212015] and ref. therein

[24] J. Rafelski, J. Letessier, J. Phys. G 30 (2004) S1 [hep-ph/0305284]; R. Stock, hep-ph/0312039

[25] H. Satz, Rep. Prog. Phys. 63 (2000) 1511 [hep-ph/0007069]

[26] T. Matsui and H. Satz, Phys. Lett. B178 (1986) 416

[27] S.S. Adler et al. (PHENIX), Phys. Rev. Lett. 91 (2003) 072301 [nuclex/0304022], Phys. Rev. Lett. 91 (2003) 072303 [nucl-ex/0306021], nuclex/0308006; J. Adams et al. (STAR Collaboration), Phys. Rev. Lett. 91 (2003) 172302 [nuclex/0305015], Phys. Rev. Lett. 91 (2003) 072304 [nucl-ex/0306024]; B.B. Back et al. (PHOBOS Collaboration), Phys. Rev. Lett. 91 (2003) 072302 [nucl-ex/0306025]; I. Arsene et al. (BRAHMS Collaboration), Phys. Rev. Lett. 91 (2003) 072305 [nucl-ex/0307003]; G. Agakichiev et al. (CERES Collaboration), Phys. Rev. Lett. 92 (2004) 032301 [nucl-ex/0303014]

[28] D. Adamová et al. (CERES Collaboration), Nucl. Phys. A 727 (2003) 97 [nucl-ex/0305002] and ref. therein

[29] M. Asakawa, U. Heinz, B. Müller, Phys. Rev. Lett. 85 (2000) 2072 [hep-ph/0003169]; S. Jeon, V. Koch, Phys. Rev. Lett. 85 (2000) 2076 [hep-ph/0003168]; for a review, see: S. Jeon, V. Koch, hep-ph/0304012

[30] http://newstate-matter.web.cern.ch/newstate-matter/

[31] G. Alexander, Rept. Prog. Phys 66 (2003) 481

[32] G. Baym, Acta Phys. Polon, B29 (1998) 1839

[33] G. Goldhaber et al., Phys. Rev. 120 (1960) 300

[34] R. Hanbury-Brown, R. Q. Twiss, Nature 178 (1956) 1046

[35] R. M. Weiner, Phys. Rept. 327 (2000) 249

[36] E. Schnederman, J. Sollfrank, and U. Heinz, Phys. Rev C48 (1993) 2462

[37] S. Chapmann, J.R. Nix, and U. Heinz, Phys. Rev. C52 (1995) 2694

[38] U. Heinz, B. Tomášik, U.A. Wiedemann, and Y.F. Wu, Phys. Lett B382 (1996) 181

[39] P. Braun-Munzinger, I. Heppe, and J. Stachel, Phys. Lett, B465 (1999) 15

[40] R. Lietava et al. (WA97 Collaboration), J. Phys. G25 (1999) 181

[41] G. J. Odyniec, Nucl. Phys. A638 (1998) 135c

[42] J. Rafelski, Phys. Lett. B262 (1991) 333; A. Bialas, Phys. Lett. B442 (1998) 449

[43] U. W. Heinz, hep-ph/0407360v1 (2004), and ref. therein

[44] Y. Le Beyec et al., Nucl. Inst. and Meth. A371 (1996) 16

[45] G. Agakichiev et al., Eur. Phys. J. C4 (1998) 231

[46] G. Agakichiev et al., Nucl. Phys. A661 (1999) 23c

[47] M.C. Abreu et al. (NA50 Collaboration), Phys. Lett. B 410 (1997) 327

[48] M.C. Abreu et al. (NA50 Collaboration), Phys. Lett. B 410 (1997) 337

[49] M.C. Abreu et al. (NA50 Collaboration), Phys. Lett. B 410 (1999) 456

[50] B. Alessandro et al. (NA50 Collaboration), Eur. Phys. C 39 (2005) 335

[51] Bearden I.G et al (NA44 Collaboration), Phys. Rev. Lett. 78 (1997) 2080

[52] Antinori F. et al (WA97 Collaboration), Eur. Phys. J. C14 (2000) 633

[53] BNL-Report, "Hunting the Quark Gluon Plasma", BNL-73847-2005 (2005)

[54] K.H. Ackermann et al. (STAR Collaboration) Phys. Rev. Lett. 86 (2001) 402

[55] J.-Y. Ollitrault, Phys. Rev. D 46 (1992) 229

[56] S.A. Voloshin, Y. Zhang, Z. Phys. C 70 (1996) 665

[57] H. Sorge, Phys. Rev. Lett. 78 (1997) 2309; H. Sorge, Phys. Rev. Lett. 82 (1999) 2048.;

[58] P.F. Kolb, J. Sollfrank, U. Heinz, Phys. Lett. B 459 (1999) 667; P.F. Kolb, J. Sollfrank, P.V. Ruuskanen, U. Heinz, Nucl. Phys. A 661 (1999) 349.]

[59] S.A. Voloshin, A.M. Poskanzer, Phys. Lett. B 474 (2000) 27.;

[60] P.F. Kolb, J. Sollfrank, U. Heinz, Phys. Rev. C 62 (2000) 054909.

[61] A. Adare, arXiv:nucl-ex/0608033v1

[62] J. Adams et al. (STAR Collaboration), Phys. Rev. C 72, 014904 (2005), and ref. therein

[63] I. Arsene et al. (BRAHMS collaboration), Phys. Rev. Lett 91 (2003) 072305

[64] J. Adams et al., Phys. Rev. Lett. 91 (2003) 172302

[65] S. S. Adler et al., Phys. Rev. C69 (2004) 034910

[66] B. Back et al., Phys. Lett. B578 (2004) 297

[67] J. W. Cronin et al., Phys. Rev. D11 (1975) 3105

[68] A. Accardi, hep-ph/0212148

[69] J. D. Bjorken, FERMILAB-PUB-82-059-THY (1982)

[70] M. Gyulassy, M. Plumer, Phys. Lett. B243 (1990) 432

[71] X.-N. Wang, M. Gyulassy, Phys. Rev. Lett. 68 (1992) 1480

[72] X.-N. Wang, M. Gyulassy, M. Plumer, Phys. Rev. D51 (1995) 3436

[73] R. Baier, Y. L. Dokshitzer, S. Peigne, D. Schiff, Phys. Lett. B345 (1995) 277

[74] R. Baier, Y. L. Dokshitzer, A. H. Mueller, S. Peigne, D. Schiff, Nucl. Phys. B483 (1997) 291

[75] R. Baier, Y. L. Dokshitzer, A. H. Mueller, D. Schiff, Phys. Rev. C58 (1998) 1706

[76] M. Gyulassy, P. Levai, I. Vitev, Phys. Rev. Lett. 85 (2000) 5535

[77] M. Gyulassy, P. Levai, I. Vitev, Nucl. Phys. B594 (2001) 371

[78] K. Adcox, et al., Phys. Rev. Lett. 88 (2002) 022301

[79] K. Adcox, et al., Phys. Lett. B561 (2003) 82

[80] S. S. Adler, et al., Phys. Rev. Lett. 91 (2003) 072301

[81] E. Wang, X.-N. Wang, Phys. Rev. Lett. 89 (2002) 162301

[82] I. Vitev, M. Gyulassy, Phys. Rev. Lett. 89 (2002) 252301

[83] M. Gyulassy, M. Plumer, M. Thoma, X. N. Wang, Nucl. Phys. A538 (1992) 37c

[84] A. Kovner, U. A. Wiedemann (2003)

[85] M. Gyulassy, I. Vitev, X.-N. Wang, B.-W. Zhang (2003)

[86] S. S. Adler, et al., Phys. Rev. Lett. 91 (2003) 072303

[87] I. Arsene, et al., Phys. Rev. Lett. 91 (2003) 072305

[88] B. B. Back, et al., Phys. Rev. Lett. 91 (2003) 072302

[89] J. Adams, et al., Phys. Rev. Lett. 91 (2003) 072304

[90] C. Adler, et al. (STAR Collaboration), Phys. Rev. Lett. 90 (2003) 032301

[91] C. Adler, et al. (STAR Collaboration), Phys. Rev. Lett. 90 (2003) 082302

[92] J. Rak, J. Phys. G30 (2004) S1309

[93] M. Chiu, Nucl. Phys. A715 (2003) 761

[94] J. Adams et al. (STAR Collaboration), Phys. Rev. Lett. 91 (2003) 072304

[95] J. Adams et al. (STAR Collaboration), Phys. Rev. Lett. 93 (2004) 252301

[96] F. Wang (STAR Collaboration), J. Phys. G30, S1299 (2004), nucl-ex/0404010.

[97] J. Adams et al. (STAR Collaboration), Phys. Rev. Lett. 95, 152301 (2005), nucl-ex/0501016

[98] B. Jacak (PHENIX Collaboration), J. Phys. Conf. Ser. 50 (2006) 22, nucl-ex/0508036

[99] F. Wang (STAR Collaboration), Nucl. Phys. A774 (2006) 129, nucl-ex/0510068

[100] N. N. Ajitanand (PHENIX Collaboration), Acta Phys. Hung. A27 (2006) 197, nucl-ex/0511029

[101] F. Wang, Nucl. Phys. A783 (2007) 157, nucl-ex/0610011

[102] L. Molnar (2007), nucl-ex/0701061

[103] M. Horner, Quark Matter (2006)

[104] J. Casalderrey-Solana J. Phys. G: Nucl. Part. Phys. 34 (2007) S345, and ref. therein

[105] H. Stoecker Nucl. Phys. A 750 (2005) 121

[106] J. Casalderrey-Solana, E. V. Shuryak, and D. Teaney, hep-ph/0602183 (2006)

[107] J. Casalderrey-Solana, E. V. Shuryak and D. Teaney, J. Phys. Conf. Ser. 27 (2005) 22

[108] S. S. Adler et al. (PHENIX Collaboration), Phys. Rev. Lett. 97 (2006) 052301

[109] J. Adams et al (STAR Collaboration), Phys. Rev. Lett. 95 (2005) 152301

[110] C. M. Hung and E. V. Shuryak, Phys. Rev. C 57 (1998) 1891

[111] G. M. Welke, R. Venugopalan, and M. Prakash, Phys. Lett. B 245 (1990) 137

[112] J. Ruppert and B. Muller, Phys. Lett. B 618 (2005) 123

[113] I. M. Dremin, JETP Lett. 30, 140 (1979) [Pisma Zh. Eksp. Teor. Fiz. 30, 152 (1979)]; I. M. Dremin, arXiv:hep-ph/0507167

[114] V. Koch, A. Majumder and X.-N. Wang, arXiv:nuclth/0507063

[115] A. Majumder and X.-N. Wang, arXiv:nucl-th/0507062

[116] C. B. Chiu and R. C. Hwa, Phys. Rev. C 74 (2006) 064909

[117] N. Armesto, C. A. Salgado, U. A. Wiedemann, Phys. Rev. Lett. 93 (2004) 242301

[118] J. Adams et al. (STAR Collaboration), Phys. Rev. Lett. 95 (2005) 152301

[119] J. Adams et al. (STAR Collaboration), Phys. Rev. C 73 (2006) 064907

[120] J. Putschke (STAR Collaboration), J. Phys. G74 (2007) S679, arXiv:nucl-ex/0701074.

[121] F. Wang (STAR Collaboration), XIth International Workshop on Correlation and Fluctuation in Multiparticle Production, Hangzhou, China, November 2007, arXiv:0707.0815

[122] J. Bielčíková (STAR Collaboration), J. Phys. G74 (2007) S929, arXiv:nucl-ex/0701047, and arXiv:0707.3100[nucl-ex]

[123] B. Abelev (STAR Collaboration), arXiv:0705.3371[nuclex]; L. Molnar (STAR Collaboration), arXiv:nucl-ex/0701061; J. Longacre (STAR Collaboration), arXiv:nucl-ex/0702008

[124] R. C. Hwa and C. B. Yang, Phys.Rev. C 67 034902 (2003); R. C. Hwa and Z. G. Tan, Phys. Rev. C 72, 057902 (2005); R. C. Hwa and C. B. Yang, nucl-th/0602024.

[125] C. B. Chiu and R. C. Hwa Phys. Rev. C 72 (2005) 034903

[126] P. Romatschke, Phys. Rev. C 75 (2007) 014901

[127] S. A. Voloshin, Nucl. Phys. A749 (2005) 287

[128] E. Shuryak, arXiv:0706.3531

[129] V. S. Pantuev, arXiv:0710.1882.; C. Y. Wong, hep-ph:0712.3282; A. Majumder et al., Phys. Rev. Lett 99 (2004) 042301

[130] http://lhc.web.cern.ch/lhc/

[131] ALICE Collaboration, J. Phys.G: Nucl. Part. Phys 32 (2006) 1295

[132] http://atlas.web.cern.ch/Atlas/GROUPS/PHYSICS/TDR/access.html

[133] CMS Collaboration, J. Phys. G: Nucl. Part. Phys 34 (2007) 995

[134] RHIC-II/eRHIC White Paper, http://www.bnl.gov/npp/docs/NSAC_RHICII-eRHIC_2-15-03.pdf

[135] http://rnc.lbl.gov/hft/

[136] PHENIX Collaboration, Nucl. Inst. and Meth. A 511, (2003) 210

[137] http://www.gsi.de/fair/experiments/CBM/index.html

[138] D.M. Alde et al., Phys. Rev. Lett. 66 (1991) 133

[139] J.A. Appel, Ann. Rev. Nucl. Part. Sci. 42 (1992) 367

[140] S. Frixione et all, hep-ph/9702287 (1997)

[141] J. Adams, et al., Phys. Rev. Lett. 94 (2005) 062301

[142] Y.L. Dokshitzer and D.E. Kharzeev, Phys. Lett. B519 (2001) 199

[143] S. S. Adler et al. (PHENIX Collaboration), Phys. Rev. Lett. 96 (2006) 032301

[144] B. I. Abelev et al. (STAR Collaboration), Phys. Rev. Lett. 98 (2007) 192301

[145] A. Adare et al. (PHENIX Collaboration), Phys. Rev. Lett. 98 (2007) 172301

[146] K. Adcox et al., Phys. Rev. Lett. 88 (2002) 022301

[147] S.S. Adler et al., Phys. Rev. Lett. 91 (2003) 072301

[148] I. Arsene et al., Phys. Rev. Lett. 91 (2003) 072305

[149] B.B. Back et al., Phys. Lett. B578 (2004) 297

[150] J. Adams et al., Phys. Rev. Lett. 91 (2003) 172302

[151] M. G. Mustafa, Phys. Rev. C 72 (2005) 014905; M. G. Mustafa, M. H. Thoma, Acta Phys. Hung. A 22 (2005) 93

[152] A. K. Dutt-Mazumder, J. Alam, P. Roy, B. Sinha, Phys Rev. D 71 (2005) 094016

[153] J. D. Bjorken, FERMILAB-PUB-82-059-THY

[154] M. Harisson et al., Nucl. Instr. and Meth. A 499 (2003) 235

[155] K. Ackermann et al., Nucl. Instr. and Meth. A 499 (2003) 624

[156] K. Adcox et al., Nucl. Instr. and Meth. A 499 (2003) 469

[157] M. Adamczyk et al., Nucl. Instr. and Meth. A 499 (2003) 437

[158] B. Back et al., Nucl. Instr. and Meth. A 499 (2003) 603

[159] The STAR Collaboration, The STAR Conceptual Design Report, June 15, 1992 LBL-PUB-5347. J.W. Harris, et al., Nucl. Phys. A 566 (1994) 277c

[160] R.L. Brown, et al., Proceedings of the 1997 IEEE Particle Accelerator Conference, 3230 (1998); F. Bergsma, et al., The STAR Detector Magnet Subsystem, Nucl. Instr. and Meth. A 499 (2003) 629

[161] The STAR Time Projection Chamber, Nucl. Instr. and Meth. A 499 (2003) 655

[162] H. Wieman, et al., IEEE Trans. Nucl. Sci. NS-44 (1997) 671

[163] M. Beddo, et al., The STAR barrell electromagnetic calorimeter, Nucl. Instr. and Meth. A 499 (2003) 751

[164] A. Schuttauf, et al., Nucl. Phys. A 661 (1999) 677c; K.H. Ackerman, et al., The Forward Time Projection Chamber in STAR, Nucl. Instr. and Meth. A 499 (2003) 709

[165] C.E. Allgower, et al., The STAR endcap electromagnetic calorimeter, Nucl. Instr. and Meth. A 499 (2003) 736

[166] J. Wu et al, J. Phys. G: Nucl. Part. Phys. 34 (2007) S729

[167] M. Aggarwal, et.al., The STAR Photon Multiplicity Detector, Nucl. Instr. and Meth. A 499 (2003) 721

[168] C. Adler, A. Denisov, E. Garcia, M. Murray, H. Strobele, S. White, The RHIC zero degree calorimeter, Nucl. Instr. and Meth. A 470 (2001) 488

[169] D. Lynn, et al., Nucl. Instr. and Meth. A 447 (2000) 264; R. Bellwied, et al., The STAR Silicon Vertex Tracker, Nucl. Instr. and Meth. A 499 (2003) 636

[170] The STAR Collaboration, STAR Project CDR Update, January 1993 LBL-PUB-5347Rev

[171] http://www.star.bnl.gov and references therein

[172] J. Thomas, et al., Nucl. Instr. and Meth. A 478 (2002) 166

[173] F. Bergsma, et al., The STAR magnet system, Nucl. Instr. and Meth. A499 (2003)

[174] A. Knospe, 24th Winter Workshop on Nuclear Dynamics (2008)

[175] G. Wang, Quark Matter 2008 proceedings

[176] http://www.star.bnl.gov/STAR/comp/simu/newsite/geometry.html

[177] K. Adcox et al.,Phys. Rev. Lett., 88 (2002) 192303, nucl-ex/0202002

[178] T. Sjostrand et al., Comput. Phys. Commun., 135 (2001) 238, hep-ph/0010017

[179] R. Rapp, Phys. Rev., C63:054907, 2001. hep-ph/0010101

[180] J. Jia, nucl-ex/0510019

[181] S.S. Adler et al. (PHENIX Collaboration), arXiv:nucl-ex/0507004